



THE UNIVERSITY *of* EDINBURGH

Edinburgh Research Explorer

Topographic Response to Horizontal Advection in Normal Fault-Bound Mountain Ranges

Citation for published version:

Hoskins, AM, Attal, M, Mudd, SM & Castillo, M 2023, 'Topographic Response to Horizontal Advection in Normal Fault-Bound Mountain Ranges', *Journal of Geophysical Research: Earth Surface*, vol. 128, no. 8, e2023JF007126. <https://doi.org/10.1029/2023JF007126>

Digital Object Identifier (DOI):

[10.1029/2023JF007126](https://doi.org/10.1029/2023JF007126)

Link:

[Link to publication record in Edinburgh Research Explorer](#)

Document Version:

Publisher's PDF, also known as Version of record

Published In:

Journal of Geophysical Research: Earth Surface

Publisher Rights Statement:

© 2023. The Authors.

General rights

Copyright for the publications made accessible via the Edinburgh Research Explorer is retained by the author(s) and / or other copyright owners and it is a condition of accessing these publications that users recognise and abide by the legal requirements associated with these rights.

Take down policy

The University of Edinburgh has made every reasonable effort to ensure that Edinburgh Research Explorer content complies with UK legislation. If you believe that the public display of this file breaches copyright please contact openaccess@ed.ac.uk providing details, and we will remove access to the work immediately and investigate your claim.





Topographic Response to Horizontal Advection in Normal Fault-Bound Mountain Ranges

A. M. Hoskins¹ , M. Attal¹ , S. M. Mudd¹, and M. Castillo² 

¹School of GeoSciences, University of Edinburgh, Edinburgh, UK, ²Instituto de Geología, Universidad Nacional Autónoma de México, Ciudad Universitaria, México

Key Points:

- Divide migration is required to balance advection and maintain spatially fixed drainage divides in steady-state landscapes with advection
- Elongate catchments and erosional disequilibrium at divides are diagnostic of strong advection, as observed in Sierra la Laguna, Mexico
- Divide migration can occur without affecting the drainage area of adjacent catchments in the presence of a high tectonic advection velocity

Supporting Information:

Supporting Information may be found in the online version of this article.

Correspondence to:

A. M. Hoskins,
a.m.hoskins-1@sms.ed.ac.uk

Citation:

Hoskins, A. M., Attal, M., Mudd, S. M., & Castillo, M. (2023). Topographic response to horizontal advection in normal fault-bound mountain ranges. *Journal of Geophysical Research: Earth Surface*, 128, e2023JF007126. <https://doi.org/10.1029/2023JF007126>

Received 17 FEB 2023
Accepted 18 JUL 2023

Abstract Tectonic displacements consist of vertical uplift or subsidence, and horizontal advection. We consider the effects of tectonic advection on mountain range topography, surface drainage patterns and drainage divides. Through numerically modeling a normal fault and uplifted footwall, we find that advection promotes the elongation of catchments and reduction in outlet spacing at mountain fronts. We demonstrate an erosional disequilibrium associated with the advection-induced transfer of mass from the proximal mountain front toward the distal mountain front. Our modeling also demonstrates the development of an erosion rate disequilibrium around fixed geomorphic features such as drainage divides, that we deem characteristic of advection. In our model, steady-state is achieved when the divide migration occurs at the same rate as advection; advection moves topography away from the fault, meaning drainage migration becomes a mechanism for balancing advection. Topographic observations in a mountain range bound by a low angle normal fault, the Sierra la Laguna (Mexico), are consistent with our modeling results when advection is included. These observations reveal a strong influence of advection on the development of the Sierra la Laguna's topography and suggest the main drainage divide is migrating toward the fault to counterbalance advection. Tectonic advection exerts a significant control on erosion rate distribution, topographic and drainage patterns and the stability of drainage divides. This work also highlights that the Gilbert metrics and across-divide χ disequilibrium cannot always be interpreted in terms of growing or shrinking catchments in settings with a large advection component of tectonic displacement.

Plain Language Summary All mountains experience tectonic motion: vertical motion (uplift or subsidence) and horizontal motion (advection). Here, we use equations that describe how features such as rivers and hillslopes change with time to model the growth of a mountain. We model displacement on a normal fault, which typically forms when the Earth's crust is stretched. We find that advection has a very strong impact on the shape of the landscape: river basins become longer and narrower when advection is faster. We also see the development of differences in erosion rates that allow the main ridgeline to migrate toward the fault at the same rate the land is moved away from the fault: at that point, the shape of the mountain is not changing anymore, despite constant advection and some places eroding much faster than others. This situation is analogous to the formation of a standing wave in a river: the wave looks static despite water moving downstream. We find similar features in the Sierra la Laguna (Mexico), including elongated catchments and evidence that the main ridgeline is actively migrating toward the fault. This helps to validate the model, and highlights that advection can make landscapes more dynamic than expected.

1. Introduction

Mountain ranges form when uplift outpaces erosion over sufficient spatial and temporal scales. Uplift is controlled by the tectonic setting, whereas erosion is governed by the geometry of surface drainage networks (e.g., Hovius, 1996; Talling et al., 1997), the ability of rivers to incise into the uplifting landscape (e.g., Whipple & Tucker, 1999), and the response from adjacent hillslopes to changes in river elevation (e.g., Hurst et al., 2012; Hurst, Mudd, Attal, & Hilley, 2013; Hurst, Mudd, Yoo, et al., 2013). A river's ability to incise is controlled by a number of factors including the local climate and the susceptibility of underlying geology to erosion. Erosion can be modulated by factors such as climate and lithology, which themselves are influenced by tectonics. A topographic steady-state marks the theoretical endpoint of a landscape's adjustment to a period during which these factors are held constant (e.g., Hack, 1960; Willett & Brandon, 2002).

© 2023. The Authors.

This is an open access article under the terms of the [Creative Commons Attribution License](https://creativecommons.org/licenses/by/4.0/), which permits use, distribution and reproduction in any medium, provided the original work is properly cited.

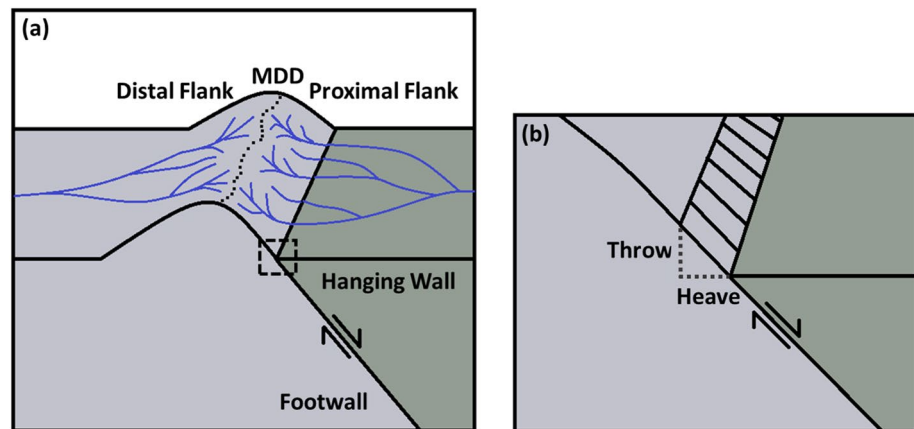


Figure 1. A sketch of a mountain range bounded by a normal fault. (a) Normal-fault bound mountain range. (b) Inset (dashed box in (a)) of mountain front with fault scarp. The footwall is uplifted relative to the hanging wall, forming a mountain range. Drainage patterns develop on the proximal (closest to the fault) and distal (furthest from the fault) flanks of the mountain range. The Main Drainage Divide marks the boundary between the proximal and distal flank surface drainages. During an earthquake, tectonic displacement along the fault occurs in a vertical (throw) and horizontal (heave) direction, as indicated by a fault scarp (striped). Over long timescales, combined earthquake displacements can be considered to produce a tectonic velocity with a vertical (uplift) and horizontal (advection) component.

In the case of a simple fault-bounded mountain range, displacement of topography is controlled by a combination of the fault dip angle and the rate of footwall slip relative to the hanging wall, as illustrated in Figure 1 with the example of a normal fault. A single earthquake or slip event produces both throw (vertical) and heave (horizontal) motion. Over timescales of landscape evolution, cumulative throw and heave can be termed uplift and advection respectively. This uplift and advection can change the topography and drainage patterns of a mountain range.

In fault-bounded mountain ranges (Figure 1), the spatial distribution of uplift has been shown to affect the symmetry of the steady-state mountain range. For example, given an uplift gradient, where the rate of uplift decreases with distance from a fault, an asymmetry across the mountain range is observed. A shorter and steeper proximal flank forms, whilst the distal flank lengthens and becomes less steep (Forte & Whipple, 2018; He et al., 2021; Whipple, Forte, et al., 2017; Zhou et al., 2022). An increase in uplift gradient induces a migration of the mountain range's Main Drainage Divide (MDD) toward the area of greater uplift (Forte & Whipple, 2018; Whipple, Forte, et al., 2017).

Advection is often omitted from studies for simplicity. However, Willett et al. (2001), describe the importance of considering both the vertical (uplift) and horizontal (advection) components of tectonic displacement, where landscapes with an advective component must balance the tectonic velocity both vertically and horizontally in order to achieve steady-state. In a setting characterized by a strong advective component, one can have relatively stable relief, as well as a relatively stable drainage divide, while tectonic advection continually moves points on the landscape relative to the drainage boundaries (e.g., Eizenhöfer et al., 2019; Miller et al., 2007; Willett et al., 2001). This can lead to continuous reorganization of drainage boundaries despite the main topographic features (e.g., relief, the MDD) remaining constant in a state of dynamic equilibrium.

Drainage reorganization has been shown to occur in response to changes in tectonics (e.g., Forte & Whipple, 2018; Hilley & Arrowsmith, 2008; Whipple, Forte, et al., 2017), precipitation (e.g., Bonnet, 2009), lithology (e.g., Bernard et al., 2021), and/or base level (e.g., Berlin & Anderson, 2007; Schwanghart & Scherler, 2020). Bishop (1995) discusses three types of drainage reorganization: (a) Capture (“bottom-up,” initiated by headwaters of the capturing channel); (b) Diversion (“top-down,” initiated by captured channel); (c) Beheading (area transfer without channel preservation). Capture and diversion tend to be instantaneous, for example, a drainage capture event which transfers a tributary and its headwaters from one catchment to another (e.g., Douglass & Schmeckle, 2007; Rowan et al., 2013; Shugar et al., 2017; Stokes et al., 2018). Beheading tends to be more gradual, for example, the progressive migration of a drainage divide (e.g., Berlin & Anderson, 2007; Schwanghart & Scherler, 2020). Catchments gaining area are termed aggressor catchments, whilst catchments losing area are termed victim catchments (Willett et al., 2014).

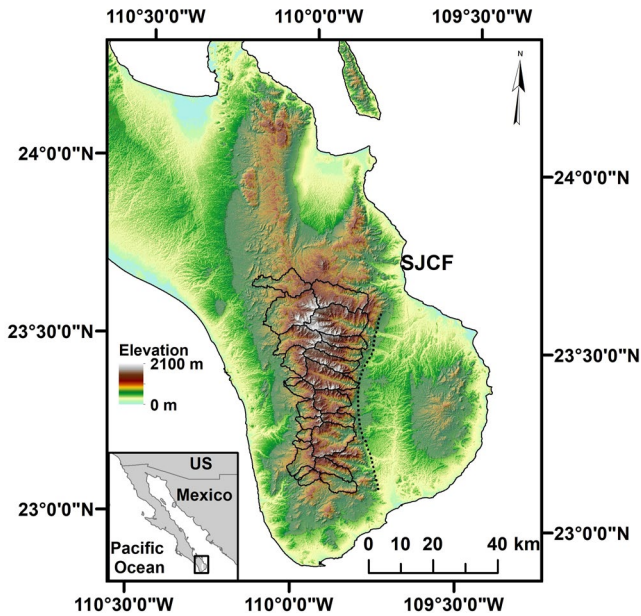


Figure 2. Map of the Sierra la Laguna, Southern Baja California Sur, Mexico. Catchments that drain the Sierra la Laguna and border the main drainage divide are shown. Areas with an elevation >250 m are overlain by a hillshade (Digital Elevation Model from the Shuttle Radar Topography Mission). The San José del Cabo normal Fault is shown as mapped based on topographic observation (dotted line).

A landscape experiencing a significant advection component at steady-state may therefore exhibit some of the features that characterize a landscape's transient response to perturbations in external forcings. The extent to which records of advection are preserved within the topography of a mountain range, and whether diagnostic features can help discriminate between these two scenarios (transient landscape vs. steady-state landscape with advection), are currently poorly understood.

The tectonic components of uplift and advection have previously been shown to exert competing controls on the shape of a mountain range. Uplift gradients promote steeper proximal flanks and less steep distal flanks, whereas faster advection has been shown to lengthen and reduce the steepness of the proximal flank, whilst shortening and increasing the steepness of the distal flank (Miller et al., 2007; Willett, 1999; Willett & Brandon, 2002; Willett et al., 2001). A change in mountain range cross-section results from the need for a steady-state mountain range to balance both the horizontal (advection) as well as the vertical (uplift) bedrock motions through erosion (Miller et al., 2007). It has also been shown that an increase in advection rate induces a migration of the MDD in the same direction as the advection velocity (He et al., 2021; Shi et al., 2021). This means the relative influence of uplift and advection will be reflected in the mountain range topography, surface drainage patterns, and channel profiles (Willett et al., 2001).

Castelltort et al. (2012) demonstrate how advection perpendicular to a fault combined with strike-slip motion along the fault results in curved drainages on the proximal flank that contain a record of the historic tectonic velocity induced by the fault. They also suggest tectonic records on the distal flank are obscured by continuous drainage reorganizations. However, Eizenhöfer

et al. (2019) refer to legacy landscapes, where advection has transferred information relating to the tectonic velocity from the proximal to the distal flank and subsequently beyond the actively uplifting mountain range. They suggest information about the tectonic past of these legacy landscapes are preserved in high-relief advection-parallel interfluges and this tectonic information can be extracted through channel slope values normalized by drainage area.

In this study, we build on this work by analyzing mountain range topography, surface drainage patterns and channel profiles that are most likely to evolve as advection and uplift rates (and therefore fault dip) are varied in a series of numerical model scenarios. We aim to distinguish between the effects of an uplift gradient and advection perpendicular to the fault, and identify topographic signals of this advection. Questions we consider for each scenario are: Is dynamic equilibrium achievable across the uplifted footwall of a low angle normal fault? Is the topographic signature of advection identifiable? And what happens to drainage divides as topography is advected away from the fault?

The inspiration for our numerical models is the Sierra la Laguna, a Cretaceous batholith (Ortega-Gutiérrez et al., 2014) forming a N-S mountain range located at the southernmost point of the Baja California Peninsula, Baja California Sur, Mexico. The Sierra la Laguna is a normal-fault bound granitoid massif with a dip angle as low as 45° (Bot et al., 2016). The range is asymmetric with a long (proximal) flank adjacent to the fault that exhibits evidence of drainage reorganization, including stream capture, beheaded catchments and dry relic channels (Bot et al., 2016). We use the Sierra la Laguna to test numerical modeling findings in a natural setting that demonstrates a high advective component of the total tectonic velocity.

2. Sierra La Laguna

2.1. Geologic and Tectonic Setting

The Sierra la Laguna is located at the southernmost point of the Baja California peninsula in Baja California Sur, Mexico (Figure 2). The Los Cabos lithospheric block underlies the Sierra la Laguna and consists of a granitoid massif of Cretaceous plutonics (Bot et al., 2016; Fletcher & Munguía, 2000; Fletcher et al., 2000). The largely

homogenous geology of the Los Cabos block makes the Sierra la Laguna an ideal study site for investigating the relative importance of uplift and advection.

The low angle normal fault, the San José del Cabo Fault (SJCF), marks the eastern extent of the Los Cabos block (Martinez-Gutierrez & Sethi, 1997). Measures of local dip angle have been as low as 45° (Bot et al., 2016). Exhumation of the Los Cabos block has been attributed to crustal thinning of Baja California related to the opening of the Gulf of California due to extensional tectonics associated with divergent North American–Pacific plate motion (Fletcher & Munguía, 2000). The absolute age of the SJCF remains unknown but the geochronology of volcanic rocks related to the extensional activity suggest the SJCF is ≈ 12 Ma structure (Duque-Trujillo et al., 2015).

Fletcher et al. (2000) extracted apatite and zircon fission-track thermochronology cooling histories for the eastern (proximal flank) and western (distal flank) margins of the Los Cabos block. Constant rapid cooling ($\approx 45^\circ\text{C Myr}^{-1}$ since the mid-Miocene; 10–12 Ma), and slow monotonic cooling ($\approx 2\text{--}3^\circ\text{C Myr}^{-1}$ since the Eocene; ≈ 56 Myr) are recorded at the margins of the eastern (proximal) and western (distal) flanks respectively (Fletcher et al., 2000). Assuming a geothermal gradient of $20\text{--}25^\circ\text{C km}^{-1}$, Fletcher et al. (2000) estimate the footwall of the SJCF has accommodated between 5.2 and 6.5 km of Neogene exhumation.

2.2. Topographic and Climatic Setting

The Sierra la Laguna displays asymmetric flanks, with a steep distal flank and a long less steep proximal flank (Bot et al., 2016). Highly elongate catchments are found on the proximal flank, whilst the distal flank displays more dendritic drainages (Figure 2). A series of wind gaps punctuate the MDD. Bot et al. (2016) document evidence of drainage reorganization, including stream capture, beheaded catchments and dry relic channels on the proximal flank.

The highest mean annual precipitation rates are ≈ 400 mm yr^{-1} (Garcillán et al., 2010). No noticeable precipitation gradients have been observed for the Sierra la Laguna; however, precipitation is thought to be greater at higher elevations. The majority of precipitation falls during intense summer storms that are related to the passage of hurricanes in the Pacific. Whilst the climate is likely to have changed over the timescale of mountain growth, the current pattern of precipitation is unlikely to be responsible for any of the drainage reorganization patterns observed due to the absence of a strong precipitation gradient.

3. Methods

3.1. Modeling Approach

To investigate the importance of uplift and advection on mountain range evolution, a series of numerical landscape evolution simulations were run using the Channel-Hillslope Integrated Landscape Development (CHILD) model (Tucker et al., 2001). The modeling scenario implemented here has been designed to identify the influence of an uplift gradient and advection on the topographic and drainage evolution of a fault-bounded mountain range. The uplift gradient is applied to mimic natural settings where uplift rate typically decreases away from a normal fault (tilted fault blocks or detachment fault with rolling hinge). The thermochronological data in the Sierra la Laguna are further evidence of such an uplift gradient (see Section 2.1).

Figure 3 summarizes the modeling scenario. The top and bottom boundaries are open (material can flux through them; their elevations are fixed), whilst the left and right boundaries are closed (i.e., no flux passes across these boundaries). The modeling scenario is defined by a window of uplift within the model domain. The bottom boundary of this window of uplift represents the location of a normal fault. The normal fault is considered fixed and acts as the absolute reference frame. Outside the window of uplift, no uplift is induced.

To simulate advection, we update the uplift field of nodes to reflect the footwall surfacing from beneath the hanging wall at the fault. This is achieved through moving the window of uplift at a constant rate (the advection rate) from the top to the bottom of the model domain as shown in stage 3 of Figure 3. All nodes remain spatially fixed in the x - y position throughout the duration of the simulation. Moving the window of uplift is equivalent to moving nodes laterally with respect to the fault.

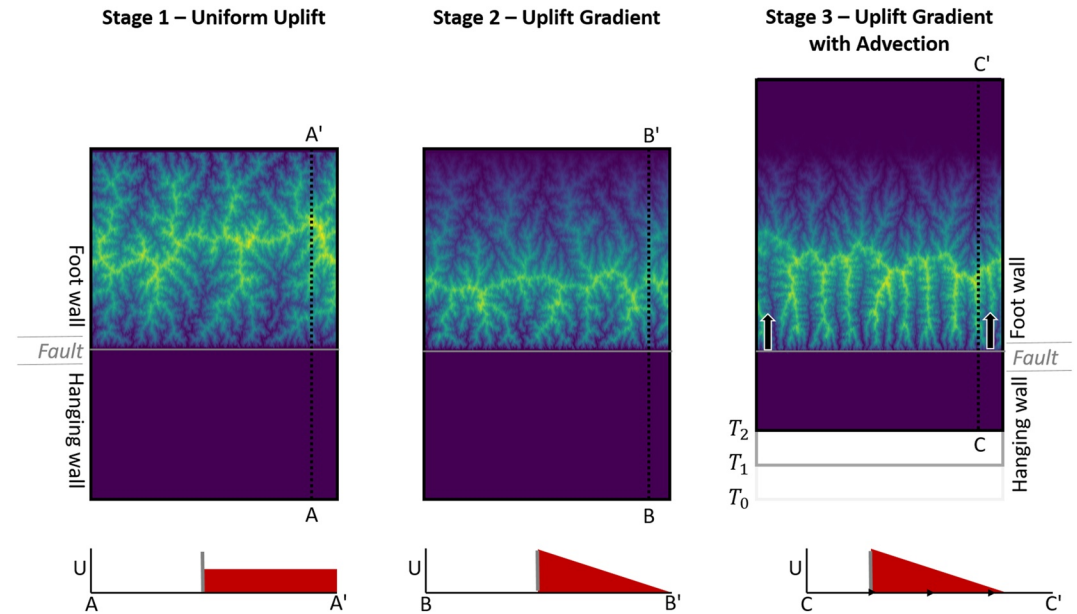


Figure 3. An illustration of the numerical model setup. Stage 1 (0–100 Myr): uniform uplift; Stage 2 (100–200 Myr): Uplift Gradient; Stage 3 (200–300 Myr) Uplift Gradient with Advection. Top is map view showing topography. Bottom is cross-section view perpendicular to the fault (shown by dashed line on map view) showing the uplift field applied (U is uplift rate). The location of the normal fault (gray) is shown at each stage. In stage 3, T_0 (200 Myr), T_1 (220 Myr), and T_2 (240 Myr) represent chronological time steps since advection is induced.

The modeling scenario consists of three phases of tectonic uplift:

1. A uniform and constant rate of uplift is applied to the window set at 0.1 mm yr^{-1} ;
2. An uplift gradient, defined by the maximum uplift rate at the fault, is applied to the window, where the uplift rate decreases linearly with distance from the normal fault to a value of 0 mm yr^{-1} at a specified distance from the fault referred to as the wedge width;
3. The window of uplift is moved across the model domain at a constant rate (the advection rate), simulating advection perpendicular to the fault, reflecting the footwall surfacing from beneath the hanging wall.

Table 1
Wedge Width, Uplift Rate at Fault, Advection Rate and Fault Dip Angles Used in Each Model Run

Model	Wedge width (km)	Uplift rate at fault (mm yr^{-1})	Advection rate (mm yr^{-1})	Fault dip angle ($^\circ$)
1	25	0.2	0.05	76
2	25	0.2	0.1	63
3	25	0.2	0.2	45
4	25	0.05	0.2	14
5	25	0.1	0.2	27
6	25	0.5	0.2	68
7	25	0.05	0.05	45
8	25	0.1	0.1	45
9	15	0.2	0.2	45
10	35	0.2	0.2	45
11	45	0.2	0.2	45

Note. The fault dip angle is conditioned by the ratio of uplift to advection rate, for example, angle = 45° when uplift rate = advection rate.

Each phase of the scenario is run for 100 Myr, with a total model run of 300 Myr. These lengthy intervals are applied to ensure the model reaches a near steady-state before the end of each phase of uplift. This suite of scenarios may seem unrealistic but it has a purpose: while it is unlikely an area will experience constant tectonic forcing for 100 Myr, or transition from uniform uplift to non-uniform uplift to non-uniform uplift with advection, modeling each phase after another provides trajectories of change that help highlight the differences between the steady-state topographies achieved at the end of each phase, which are the focus of our analysis.

Uplift gradient, surface advection and wedge width are varied independently (Table 1). Uplift rate at the fault is varied between 0.05 and 0.5 mm yr^{-1} to replicate a range of tectonic fault velocities. Advection rate is varied between 0.05 and 0.2 mm yr^{-1} , to replicate fault dip angles varying between 14° and 76° for the associated range of uplift rates (Table 1). Wedge width is varied between 15 and 45 km, varying around the approximate width of the Sierra la Laguna (25 km). When advection rate is varied, the uplift gradient (maximum uplift rate at the fault) is set to 0.2 mm yr^{-1} and the wedge width is set to 25 km (simulations 1–3). When uplift rate at the fault is varied, surface advection rate is set to 0.2 mm yr^{-1} and wedge width is set to 25 km

Table 2
The Parameters Used to Simulate Fluvial Erosion and Hillslope Sediment Flux

Parameter	Value
k_{br}	$2 \times 10^{-5} \text{ mPa}^{-1.5} \text{ yr}^{-1}$
τ_c	0 Pa
p_b	1.5
m_b	1
n_b	1
K_w	$10 \text{ m}^{-0.5} \text{ s}^{0.5}$
D	$0.001 \text{ m}^2 \text{ yr}^{-1}$
S_c	0.58
ω	0.5

(simulations 3–6). When the wedge width is varied, both uplift and surface advection rates are set to 0.2 mm yr^{-1} (simulations 9–11). As the ratio of vertical uplift rate to horizontal advection rate is a function of the fault's dip angle, the sets of simulations 1–3 and 3–6 (as well as the pairs 1 and 7, 4 and 7, 5 and 8, and 2 and 8) test the influence of the fault's dip.

The model uses a detachment-limited law to simulate fluvial erosion, where the fluvial erosion rate E is calculated as:

$$E = K_{br}(\tau_0 - \tau_c)^{p_b} \quad (1)$$

$$\tau_0 = K_t(Q/W)^{m_b} S^{n_b} \quad (2)$$

$$W = K_w Q^\omega \quad (3)$$

where K_{br} is the erodibility coefficient, τ_0 is the bed shear stress, τ_c is the critical bed shear stress below which no erosion occurs, Q is water discharge, W is channel width and p_b , K_t , K_w , m_b , n_b , and ω are constants. Q is calculated as the product of the precipitation rate and drainage area computed for

each model node at each time step; the effects of infiltration and evapotranspiration are neglected. We assume a simple hydraulic scaling and set ω to 0.5 (Attal et al., 2008). The parameters in Equations 1 and 2 can be adjusted to mimic different versions of the popular Stream Power Incision Model (SPIM) (Attal et al., 2008; Howard et al., 1994; Seidl & Dietrich, 1992; Whipple & Tucker, 1999). The SPIM can be written as:

$$E = KA^m S^n \quad (4)$$

where K is an erodibility coefficient (similar to K_{br} but incorporating the influence of a wider range of processes), A is drainage area and m and n are the area and slope exponents (Howard & Kerby, 1983; Lague, 2014). The m/n ratio controls the relationship between slope and drainage area and therefore how concave a channel is. In some circumstances, it is equivalent to the concavity index θ that is typically extracted from topographic analysis (see discussion in Section 3.2.4). For example, in a landscape where K and E are constant (e.g., uniformly uplifted landscape with uniform lithology at steady-state), Equation 4 can be rearranged to show that the concavity index θ which is defined as the gradient of the linear fit of $\log(S) = f(\log(A))$ is equal to m/n . While the value of θ varies over a wide range in nature, its median is around 0.5 (Gailleton et al., 2021; Tucker & Whipple, 2002; Whipple, 2004). Additionally, there is growing theoretical and empirical evidence that the n exponent should be greater than unity, typically closer to 2 (e.g., Adams et al., 2020; Harel et al., 2016; Lague, 2014).

Based on Equations 1–3 and assuming $\tau_c = 0$ and that discharge scales with drainage area (which is the case in our model), the exponents m and n can be derived as:

$$m = (1 - \omega)m_b p_b \quad (5)$$

$$n = n_b p_b \quad (6)$$

We set $m_b = n_b = 1$ and K_t equals the unit weight of water so that the quantity τ_0 represents the stream power per unit bed area. We then set $p_b = 1.5$ so that $n > 1$ ($n = 1.5$) and $m/n = 0.5$. We do not consider the influence of regolith, and consider that the landscape is made of bedrock.

Nonlinear hillslope diffusion is applied using a nonlinear flux law where the sediment flux q_s is given by:

$$q_s = \frac{D \nabla z}{1 - \left(\frac{|\nabla z|}{S_c}\right)^2} \quad (7)$$

where D is hillslope diffusivity, ∇z is the topographic gradient, and S_c is the critical hillslope gradient above which hillslope flux becomes infinite (Roering et al., 1999, 2001). This means hillslope sediment flux increases almost linearly at low gradient, and increases rapidly as the gradient approaches S_c .

The input parameter values used here are summarized in Table 2.

Precipitation is considered to be both spatially and temporally uniform and is set to 2.5 m yr^{-1} . The actual value used has little impact on the outcome of the model, as the efficiency of erosion processes is a trade-off between

the precipitation rate and the erodibility coefficient K_{br} for which no constraint exists; the model is calibrated to produce relief comparable to that of the Sierra la Laguna. Landscape evolution is calculated at intervals of 5 kyr and uplift rates are updated at intervals of 100 kyr. For comparison, this equates to a 20 m horizontal movement of the window of uplift between uplift rate updates when advection is induced at 0.2 mm yr^{-1} . Nodes are randomly spaced with an average node spacing of 200 m and the position of these nodes remains the same throughout the model run. Each model uses a 50 km length irregular triangular mesh to simulate mountain range evolution, and the width of the wedge and total amount of surface advection applied in each scenario defines the width of each simulations mesh.

3.2. Modeling Analysis and Comparison to the Sierra La Laguna

We analyze the modeling results to understand the relative influences of an uplift gradient and surface advection on mountain range topography and surface drainage. We consider the role played by drainage reorganization in balancing the advective component of normal faults. We also focus on the differences in topography, drainage patterns and channel characteristics between the uplift gradient and uplift gradient with advection phases of the modeling, where these changes develop in direct response to inducing advection. Further, we compare the modeled topographies with advection to that from the Sierra la Laguna. The topographic and channel characteristic analyses of the Sierra la Laguna are derived from ASTER GDEM and ALOS W3D30 data, respectively, each with a resolution of 30 m. A series of metrics are analyzed, which can be grouped in the following categories (more details are provided for each of the metrics in the following subsections):

1. *Mountain Range Asymmetry*: We extract elevation cross-sections, and analyze their shape in relation to spatial variations in uplift and erosion rates across the mountain range.
2. *MDD Dynamics*: We derive the normalized location of the MDD between mountain fronts, and compare across-MDD headwater Gilbert metrics (elevation, slope and relief) and χ values, to infer divide migration.
3. *Drainage Patterns*: We quantify the evolution of drainage networks and catchments through the spacing ratio.
4. *Channel Characteristics*: We use longitudinal profiles, χ profiles, channel steepness (K_{sn}) and channel concavity (θ) values to identify evolutionary patterns.

3.2.1. Mountain Range Asymmetry

The mean cross-section of the entire mountain range is calculated at each time step for each model run. Comparing cross-sections between model runs, and with a cross-section of the Sierra la Laguna, helps us to understand how an uplift gradient and advection combine to influence mountain range asymmetry, and whether the Sierra la Laguna exhibits some of the diagnostic features of advection.

We also analyze the balance between vertical uplift and erosion along mountain range cross-sections to assess the nature of the apparent equilibrium at the end of each modeling phase.

3.2.2. Main Drainage Divide (MDD) Dynamics

The location of the MDD is identified for each time step by identifying the upslope contributing area of all catchments draining to the top (distal flank) and bottom (proximal flank) open boundaries of the model. Where these areas meet depicts the MDD. This means we can track the location of the MDD in response to inducing an uplift gradient and then advection. The normalized location of the MDD across the width of the mountain range has previously been used to describe changes in its location (He et al., 2021; Zhou et al., 2022). Here the normalized location of the MDD is calculated at each time step following:

$$\frac{D_p}{(D_p + D_d)} \quad (8)$$

where D_p and D_d are the mean distances between the MDD and the mountain front on the proximal and distal flanks of the mountain range, respectively. Here we define the mountain front as the nearest nodes to the mountain range where the uplift rate is 0 mm yr^{-1} . The advantage of normalization is that it allows us to compare simulations with different mountain range widths, which will result from differences in wedge width, uplift gradient and advection rate.

In natural landscapes where divide migration occurs too slowly to observe in real time, a series of topographic metrics can be used to identify the relative direction of divide migration. The Gilbert metrics, after Gilbert's law

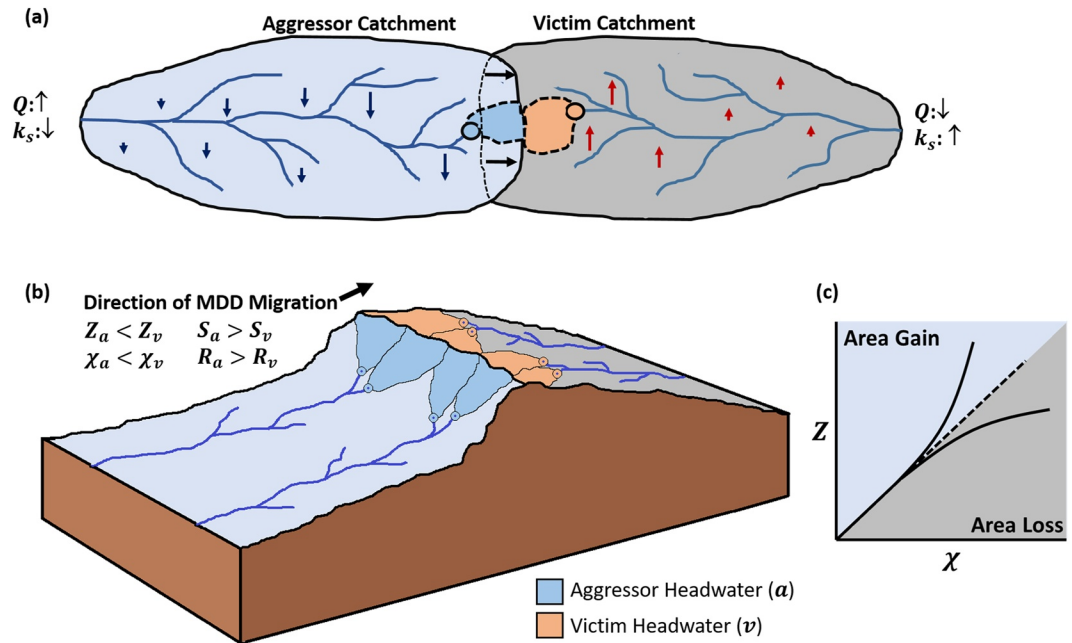


Figure 4. A conceptual illustration of the features associated with divide migration. (a) Aerial illustration of the effect of divide migration on discharge (Q) and channel steepness (k_s). (b) Oblique illustration of across-Main Drainage Divide (MDD) topographic Gilbert metrics and expected associated divide migration. (c) River profiles in χ -elevation space resulting from divide migration. The landscape in this illustration is being actively uplifted. Aggressor and victim catchments are shown in blue and gray respectively. The headwaters of aggressor (a) and victim (v) catchments are shown in blue and orange respectively. Black arrows indicate a migration of the MDD resulting from divide migration or drainage capture. Q is expected to increase in the aggressor and decrease in the victim catchment. Blue and red arrows indicate expected vertical changes in elevation as a result of the capture (increase in elevation where uplift rate outpaces erosion rate, and vice-versa). Note that the relative change in Q as a result of divide migration decreases downstream, meaning the greatest change is observed in the headwaters. A positive feedback exists; increased Q in the aggressor catchment leads to an increase in channel incision rate, whereas decreased Q in the victim catchment leads to a decrease in channel incision rate, promoting further divide migration. A negative feedback exists too; a decrease in k_s is expected in the aggressor catchment, whereas an increase in k_s is expected in the victim catchment, limiting further divide migration. This change in k_s occurs as a result of a change in catchment length without changing total relief. Higher elevation (Z) and χ values are found in the headwaters of victim catchments, whereas higher slope (S) and relief (R) values are found in the headwaters of the aggressor catchments (Forte & Whipple, 2018; Whipple, Forte, et al., 2017). χ -elevation profiles that curve toward the y axis are indicative of aggressor catchments, whilst χ -elevation profiles that curve toward the x axis are indicative of victim catchments (Willett et al., 2014; Yang et al., 2015).

of unequal declivities (Gilbert, 1877), include elevation, slope and relief (Forte & Whipple, 2018). As described in Figure 4, higher elevations are expected within the headwaters of the victim catchment (catchment losing area), whilst greater slope and relief values are expected within the headwaters of the aggressor catchment (catchment gaining area); the variables are partly interdependent, in the sense that higher headwater elevation should lead to lower relief and slope, and offer a simple way to strengthen the outcome of the analysis in naturally noisy systems. All else equal, greater slope and relief should lead to enhanced incision (Forte & Whipple, 2018; Gilbert, 1877; Whipple, DiBiase et al., 2017). Geometry dictates that the divide will migrate toward the more slowly eroding side, leading to the aggressor/victim situation.

The χ value, which normalizes streamwise distance by the stream's drainage area (Perron & Royden, 2013; Royden et al., 2000), can also be used to infer divide migration. As shown in Figure 4, higher χ values are expected on the side of the divide losing area and the curvature of channel profiles in χ -elevation space (Figure 4c) has been shown to indicate catchment area gain and loss (Beeson et al., 2017; Guerit et al., 2018; Willett et al., 2014; Yang et al., 2015).

Across-divide differences between headwater basin pairs for the Gilbert metrics (ΔZ , ΔS , and ΔR), χ values ($\Delta \chi$), and observed erosion rates (ΔER) are calculated at each time step as:

$$\Delta Z = \frac{\sum Z_d}{n_d} - \frac{\sum Z_p}{n_p} \quad (9)$$

$$\Delta S = \frac{\sum S_p}{n_p} - \frac{\sum S_d}{n_d} \quad (10)$$

$$\Delta R = \frac{\sum R_p}{n_p} - \frac{\sum R_d}{n_d} \quad (11)$$

$$\Delta \chi = \chi_d - \chi_p \quad (12)$$

$$\Delta ER = \frac{\sum ER_p}{N_p} - \frac{\sum ER_d}{N_d} \quad (13)$$

where the means of elevation (Z), slope (S) and relief (R) of all raster cells (n) in each headwater basin on the proximal (p) and distal (d) flanks are calculated for each unique headwater pair. Slope values are calculated for each cell using a 3 by 3 moving window and applying the average maximum technique (Burrough & McDonnell, 1998). Relief values are calculated by subtracting the minimum elevation from the maximum elevation within a 200 m radius of each cell. We define headwater basins as having a contributing area of $\approx 0.1 \text{ km}^2$ that are connected to the MDD. χ values are extracted at the outlet of headwater basins. Mean erosion rates (ER) of all nodes (N) are calculated in the same way. All differences are calculated such that positive ΔZ , ΔS , ΔR , $\Delta \chi$, and ΔER values reflect an expected migration of the MDD away from the fault, whereas negative values reflect an expected migration of the MDD toward the fault. To account for spatial variations along the MDD, in particular in the natural landscape (e.g., Sierra la Laguna), we perform a paired analysis, whereby headwater basins on each flank are matched with the nearest headwater basin on the opposite flank and analyzed accordingly.

We note that this calculation of ΔZ uses the mean Z of headwater cells, rather than a single value of Z from the channel head at the outlet as has previously been used to calculate Gilbert metrics (Forte & Whipple, 2018). We chose to use the mean Z in the headwaters, to encompass hillslopes and reflect the volume of material in the landscape that exists within these headwaters.

We apply the same metrics across the MDD in the Sierra la Laguna and subsequently compare these to the numerical modeling results.

3.2.3. Drainage Patterns

Drainage networks with an upslope contributing area $>0.1 \text{ km}^2$ and catchments $>5 \text{ km}^2$ are extracted using LSDTopoTools (Mudd, Clubb, et al., 2022). Drainage networks are extracted when drainage area is $>0.1 \text{ km}^2$ as this guarantees the predominance of fluvial processes over hillslope processes (Montgomery & Foufoula-Georgiou, 1993). Catchments that do not form part of the MDD are excluded from the analysis and are considered to form triangular facets (or faceted spurs) along the mountain front.

Channel outlet spacing (s), the mean distance between channels at the mountain front, and flank width (w), the mean distance between the MDD and the mountain front, have been shown to form a linear relationship on linear mountain belts, whereby s increases as w increases (Hovius, 1996). The spacing ratio (r) defined as the ratio between w and s is used to characterize the typical shape of catchments on a flank (Hovius, 1996; Talling et al., 1997). w , s , and r are calculated for the modeled topographies and for the Sierra la Laguna.

$$r = \frac{w}{s} \quad (14)$$

Higher r values represent long and narrow catchments, whereas lower r values represent short and wide catchments.

3.2.4. Channel Characteristics

Channel longitudinal profiles, channel profiles normalized by drainage area (χ profiles), normalized channel steepness index (k_{sn}) values and channel concavity index (θ) values are extracted to quantitatively characterize the topography. All channel metrics displayed here are derived through LSDTopoTools (Mudd, Clubb, et al., 2022) using algorithms of Mudd et al. (2014) to calculate k_{sn} and Mudd et al. (2018) to calculate θ . For the modeling results, CHILD output point data were used to produce a 100 m resolution DEM to perform the analyses.

An accurate χ transformation (Perron & Royden, 2013; Royden et al., 2000) or calculation of k_{sn} requires using a reference channel concavity (θ_{ref}) value. Before making a choice, it is important to consider the two potential

meanings of the channel concavity index θ . The value of θ can reflect how concave a river is, that is, how quickly slope increases as drainage area decreases upstream: this “apparent” θ is the slope of the regression line in a log-log plot of channel slope as a function of drainage area, and it can therefore be deduced from simple slope-area analysis of topographic data or, better, from χ analysis of the same data transformed to normalize for drainage area and do away with noisy slope-area data (Mudd et al., 2018; Perron & Royden, 2013; Royden et al., 2000; Wobus et al., 2006).

As mentioned in Section 3.1, θ also theoretically represents the m/n ratio in the SPIM, where m and n are the drainage area and slope exponents, respectively (Howard & Kerby, 1983; Lague, 2014). This means we know the theoretical value of θ for our model runs ($\theta = 0.5$). The apparent and theoretical θ values will be the same when uplift is uniform, and they can easily be extracted from topographic analysis, as described above. In such a case, Kirby and Whipple (2001) demonstrate how θ can be used to infer spatial variations in tectonic uplift rates.

An uplift gradient will distort the results. For example, in the case of a fault-bounded block with uplift rate decreasing away from the fault (e.g., stage 2 in our model, Figure 3), we will observe contrary effects on the proximal and distal sides of the mountain range. On the proximal side, rivers will steepen more slowly upstream compared to a case with uniform uplift, as the uplift rate will generally decrease upstream and so the slope needed to produce an erosion rate matching the uplift rate will be less compared to a uniform uplift scenario. The opposite will occur on the distal side. As a result, channels are expected to appear more concave on the distal side and less concave on the proximal side, whereas they would display identical concavity if uplift were uniform (Miller et al., 2007).

The addition of advection, as the horizontal component of tectonic motion, will complicate any uplift signal derived from θ or k_{sn} further (Kirby & Whipple, 2001). The horizontal transfer of material through advection across the mountain range will change the pattern of erosion, such that erosion does not equal uplift at all points within the landscape (Willett et al., 2001), and this will affect the characteristics of the channels. k_{sn} and θ have previously been found to be higher on the distal flank relative to the proximal when advection acts on a landscape (Miller et al., 2007; Mitchell & Forte, 2023), reflecting a change in erosion where erosion is faster on the distal flank relative to the proximal flank. Here we will test the significance of this signal in determining the influence of advection on a natural landscape when an uplift gradient and advection coexist.

As χ and k_{sn} are sensitive to θ_{ref} (e.g., Gailleton et al., 2021) and because we want to be able to compare the modeling results with the topographic analysis of the Sierra la Laguna, the same value is chosen for the analysis of both modeled and natural landscapes. Because we know the theoretical value of θ in our model, we set $\theta_{ref} = 0.5$ to calculate χ and k_{sn} .

In addition, because we want to assess the impact of uplift gradient and advection on measured θ , we calculate θ in each catchment through both slope-area methods and collinearity methods based on transformed χ values (disorder method in Mudd et al. (2018)). The former should provide an apparent θ , whereas the latter is expected to provide values closer to the true theoretical value, although the method has been developed for uniform uplift and lithology. In the following, we observe how varying the uplift gradient and advection rate leads to deviation from the theoretical value of 0.5 in the modeled landscapes, and compare these to observations from the Sierra la Laguna.

4. Results

An example of the near steady-state landscape produced at the end of each phase of uplift is shown in Figure 5. Movie S1 also shows the evolution of the landscape over the whole duration of one of the runs (through each of the three phases).

Figure 2 shows a map of the topography of the Sierra la Laguna alongside the extracted catchments. We only extract features above 300 m elevation to remove depositional features such as alluvial fans from the analysis. In total, 11 proximal (eastern) and 13 distal (western) flank catchments are extracted for the Sierra la Laguna.

4.1. Mountain Range Asymmetry

Cross sections of modeled mountain ranges as the uplift field is changed are shown in Figure 6.

Figure 6a shows the cross-sections at the end of each stage of uplift (uniform uplift, uplift gradient, and uplift gradient with advection) for a single model run. The uniform uplift phase of the model produces a largely symmetrical cross-section, whilst the uplift gradient and uplift gradient with advection phases produce asymmetrical

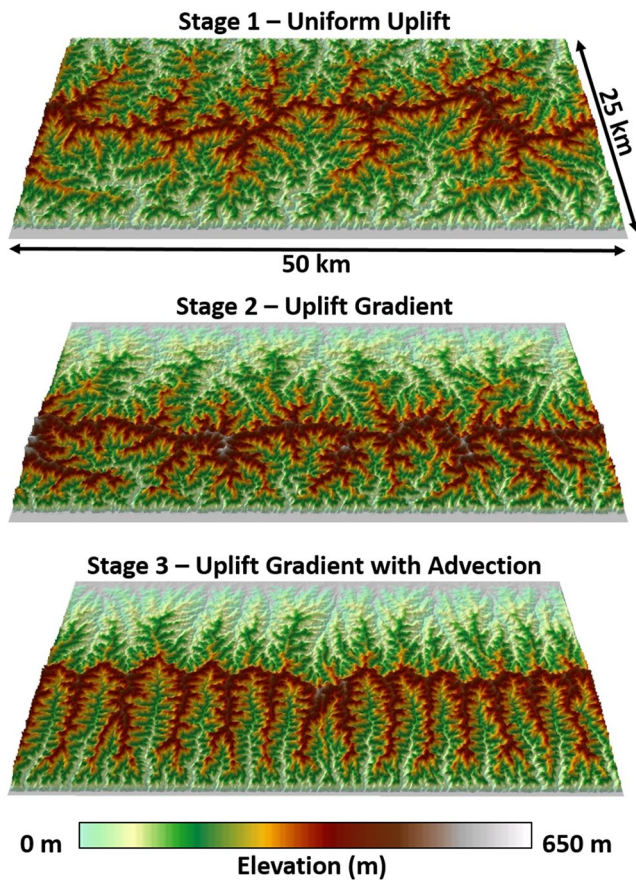


Figure 5. Near steady-state landscape at the end of each phase of uplift: (a) uniform uplift (0.1 mm yr^{-1}), (b) uplift gradient (0.2 mm yr^{-1}), (c) uplift gradient (0.2 mm yr^{-1}) with advection (0.2 mm yr^{-1}). Only the section of the model domain actively being uplifted in each stage is shown here, with the fault at the bottom of each domain. The area of active uplift is 50 km by 25 km.

cross-sections. The difference in flank width is more pronounced with only an uplift gradient.

Whilst an uplift gradient promotes a shortening of the proximal flank and a lengthening of the distal flank (Figure 6c), advection is found to promote the opposite (Figure 6b). In both uplift gradient cases (with and without advection), the distal flanks are identical at a given distance from the MDD (Figure 6a); the same is observed when advection rate is varied (Figure 6b). This means most of the changes in mountain range cross-section that occur in response to a change in the advection rate are observed on the proximal flank and in the headwaters of the distal flank.

A comparison of Figures 6c and 6d demonstrates the influence of advection on mountain range asymmetry. For each uplift gradient (Figure 6c), the inclusion of advection (Figure 6d) moves the MDD away from the fault. It additionally produces a cross-section where the headwaters of the distal flank are visibly steeper than those of the proximal flank. The magnitude of the uplift gradient, in combination with the advection rate, controls the extent to which the MDD migrates away from the fault when advection is induced (Figure 6d). However across-MDD differences in flank profiles are greater as the rate of advection is increased (Figure 6b).

A cross-section of the Sierra la Laguna is shown in Figure 7. The cross-section displays a visually more convex proximal flank and a more concave distal flank.

We show cross-sections of elevation, vertical uplift rate, and vertical erosion rate for the numerical model run with an uplift gradient of 0.2 mm yr^{-1} and an advection rate of 0.2 mm yr^{-1} in Figure 8. The ratio of the uplift rate U to the erosion rate E , U/E , is also shown.

Vertical uplift rate is balanced by vertical erosion rate at all points along the cross-sections in the uniform uplift (Figure 8a) and uplift gradient (Figure 8b) scenarios. However, in the uplift gradient with advection scenario (Figure 8c), $U > E$ on the proximal flank, whilst $U < E$ on the distal flank, displaying spatial disequilibrium between uplift and erosion across the mountain range, in particular near the MDD. This occurs while topography is at steady-state, that is, invariant when using the fault position as a reference.

4.2. MDD Dynamics

4.2.1. MDD Migration

The normalized location of the MDD is shown for the duration of each model run in Figure 9. In each model run during the uniform phase of uplift, the location of the MDD stabilizes near a normalized value of 0.5, equidistant from both the proximal and distal flank mountain fronts.

In each model run, once the uplift gradient is induced at 100 Myr, the MDD preferentially migrates toward the fault. The rate and extent of this migration systematically changes with the magnitude of the uplift gradient induced (Figure 9a), whereby the steeper the uplift gradient, the faster and the further the MDD migrates toward the fault.

Conversely, in each model run, once advection is induced at 200 Myr, the MDD preferentially migrates away from the fault. Similarly, the rate and the extent of this migration systematically change with the rate of advection (Figure 9b), whereby the faster the advection, the faster and further the MDD migrates away from the fault.

Changes in the wedge width do not appear to systematically change how the MDD responds to either an uplift gradient or advection (Figure 9c).

The tectonic velocity however, that is, the rate of displacement on the fault (including both vertical and horizontal component), seems to control the location of the MDD at the end of the uplift gradient with advection phase. This is shown in Figure 9d where the location of the MDD is compared for runs with different tectonic velocities but the same dip angle of the normal fault ($=45^\circ$, i.e., uplift rate = advection rate). A slower tectonic velocity results

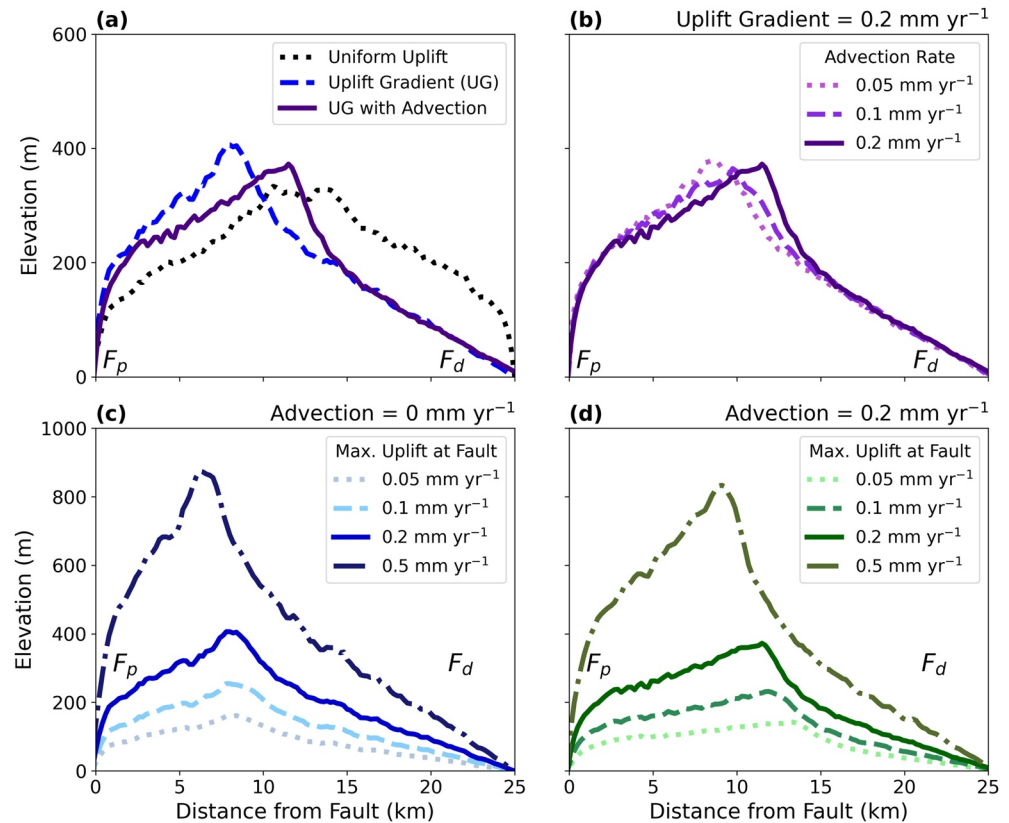


Figure 6. Model cross-sections orthogonal to the fault. The patterns shown here are representative of all model runs. (a) Cross-section of model at near steady-state: uniform uplift at 100 Myr (uplift = 0.1 mm yr⁻¹), linear uplift gradient at 200 Myr (maximum uplift = 0.2 mm yr⁻¹), and linear uplift gradient with advection at 300 Myr (maximum uplift = 0.2 mm yr⁻¹ and advection = 0.2 mm yr⁻¹). (b) Cross-section of models at 300 Myr as advection rate is varied (0.05, 0.1, 0.2 mm yr⁻¹). (c) Cross-sections with no advection (at 200 Myr) as uplift gradient is varied (0.05, 0.1, 0.2, 0.5 mm yr⁻¹). (d) Cross-sections with advection set to 0.2 mm yr⁻¹ (at 300 Myr) as uplift gradient is varied (0.05, 0.1, 0.2, 0.5 mm yr⁻¹). F_p and F_d indicate the proximal and distal mountain flanks respectively. The entire area being actively uplifted is used to calculate these cross-sections.

in the uplift gradient exerting greater control over the normalized location of the MDD (i.e., the divide stabilizes closer to the proximal mountain front), whereas a faster tectonic velocity results in advection exerting greater control over the normalized location of the MDD (i.e., the divide stabilizes closer to the distal mountain front).

4.2.2. Across-MDD Gilbert Metric and χ Comparisons

Across-MDD Gilbert metric and χ values are calculated every 10 Myr between 80 and 300 Myr (Figure 10). Here the differences in across-MDD Gilbert metrics and χ values have been calculated such that positive and negative ΔZ , ΔS , ΔR , and $\Delta \chi$ values are expected to reflect higher erosion rates in the headwaters of catchments draining the proximal and distal flanks, respectively. Where ΔZ , ΔS , ΔR , and $\Delta \chi$ values are 0, erosion rates in the headwaters of the proximal and distal flanks are expected to be equal.

At the end of the uniform uplift phase of the model, the across-MDD Gilbert metric comparisons display mean values close to 0 (Figures 10a–10c), meaning across-MDD erosion rates are similar and the MDD is unlikely to be migrating in either direction, corroborated by the actual lack of divide migration observed (Figure 9), and observed across-MDD differences in ER, ΔER (Figure 10e).

The first calculation of the Gilbert metrics after the uplift gradient is induced occurs at 110 Myr. Here, virtually all ΔZ , ΔS , and ΔR values are negative, indicating higher erosion rates in the headwaters of the distal flank. Such disequilibrium in across-MDD erosion rates is expected to lead to a migration of the MDD toward the fault. As time passes, across-MDD Gilbert metric comparisons progressively return to values closer to 0, indicating erosion rates on either side of the MDD are becoming similar. This is reflected in observed erosion rates (Figure 10e).

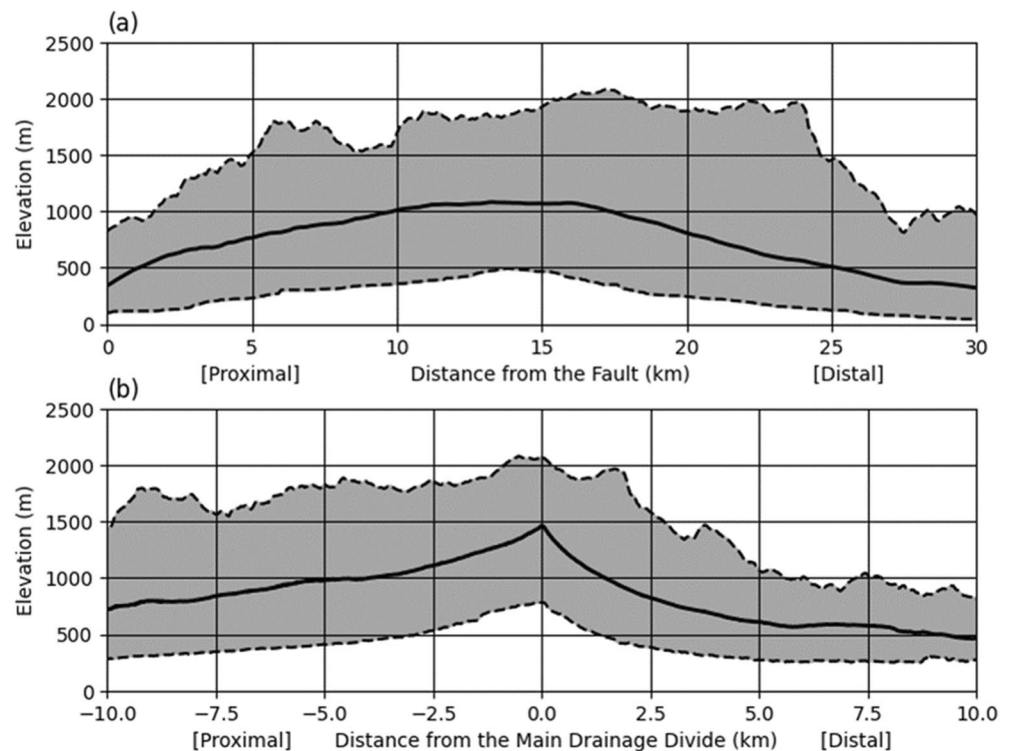


Figure 7. Cross-sections of the Sierra la Laguna. (a) Cross-section derived using distance from the fault (SJCF), including all topography. (b) Cross-section derived using distance from the Main Drainage Divide (MDD), and exclusively using topography within catchments that border the MDD. (a) Reflects how topography varies with distance from the fault, where the fault is assumed to represent the location of material input into the landscape. (b) Reflects across-MDD differences in topography. For each cross-section the mean (solid), minimum and maximum (dashed) elevation values are shown. The entire mountain range is used to calculate the cross-section in (a). Catchments bordering the MDD are used to calculate the cross-section in (b); this means triangular facets are removed from the calculation in (b).

When advection is induced at 200 Myr, the across-MDD Gilbert metric comparisons again indicate faster erosion in the headwaters of the distal flank. This difference in erosion rates across the MDD is strongest around 230 Myr (Figures 10a–10c). However, in contrast to the uplift gradient only scenario, where ΔZ , ΔS , and ΔR values returned closer to 0 with time, these values remain largely constant and strongly negative when advection is modeled. These values are indicative of consistently higher erosion rates in the headwaters of the distal flank, and should lead to continual migration of the MDD toward the fault. Again, this is reflected in observed erosion rates (Figure 10e).

Across-MDD χ comparisons ($\Delta\chi$) however exhibit signals that are inconsistent with our expectation. ΔER values show no erosional disequilibrium at the end of the uplift gradient phase; there is a strong across-divide erosional disequilibrium at the end of the uplift gradient with advection phase, suggesting distal catchments are aggressors (Figure 10e). $\Delta\chi$ values are positive during the uplift gradient phase of the modeling, suggesting distal catchments are victims, and sit near 0 during the uplift gradient with advection phase (Figure 10d). We note however that $\Delta\chi$ values do track the pattern of ΔER values after advection is induced (Figure 10). These discrepancies may result from the fact that analyses of across-divide χ disequilibrium typically rely on the assumptions of uniform lithology (which is fulfilled here), uniform uplift (which is breached here), and using a common base level and avoiding zones of subsidence and/or active deposition for all analyzed catchments (which is fulfilled in the model but is not in the Sierra la Laguna) (Perron & Royden, 2013; Whipple, Forte, et al., 2017).

The across-MDD Gilbert metric and χ comparisons for the Sierra la Laguna are shown in Figure 11. All three of the Gilbert metrics indicate higher erosion rates in distal flank headwaters. The χ comparison indicates the opposite.

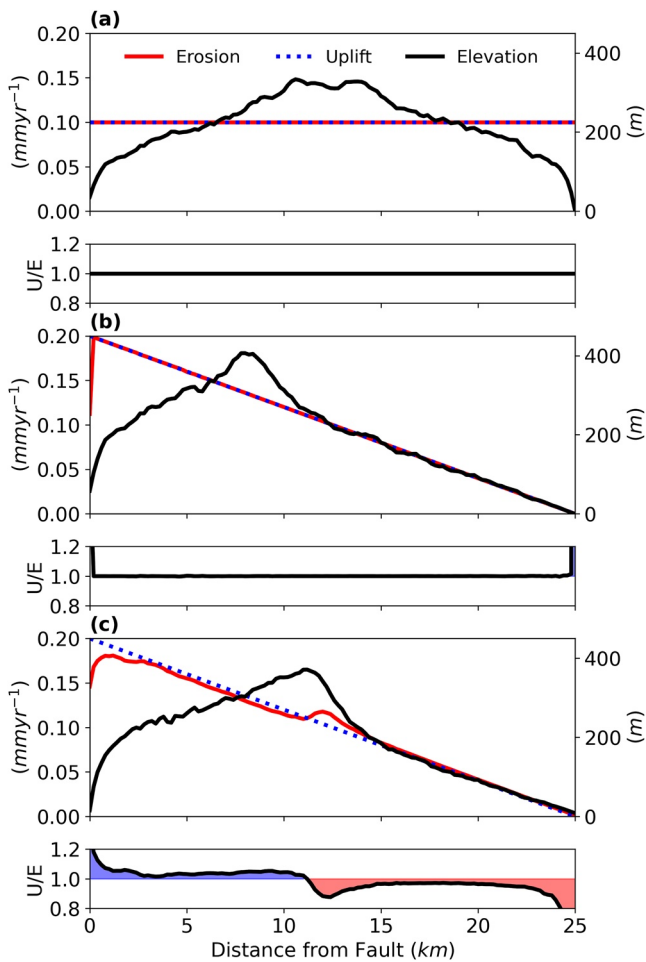


Figure 8. Model cross-sections orthogonal to the fault during: (a) Uniform uplift, (b) Uplift gradient, (c) Uplift gradient with advection. Mean elevation (black), vertical uplift rate (dashed blue) and vertical erosion rate (red) are plotted by distance from the fault. The balance between the uplift rate (U) and erosion rate (E) are plotted as (U/E), such that values >1 reflect excess uplift (shaded blue) and values <1 reflect excess erosion (shaded red). The data presented here relates to the numerical model run with a uniform uplift rate of 0.1 mm yr^{-1} in (a), an uplift gradient of 0.2 mm yr^{-1} in (b), and an uplift gradient of 0.2 mm yr^{-1} with an advection rate of 0.2 mm yr^{-1} in (c). The data plotted here are extracted from the numerical modeling at 95 Myr (a), 195 Myr (b), and 295 Myr (c); these time steps are deemed to represent near steady-state landscapes.

The differences are clearer when looking at channel χ profiles: profiles on the proximal flank (Figure 13c), become steeper in response to the uplift gradient and are slightly convex, meaning k_{sn} decreases upstream, as expected since the uplift rate generally decreases upstream (i.e., away from the fault). Conversely, the χ profiles on the distal flank (Figure 13d), become less steep in response to the uplift gradient and are concave up, meaning k_{sn} increases upstream; again, this is expected, as uplift rate generally increases upstream on this flank (i.e., toward the fault). Once advection is induced, proximal flank χ profiles (Figure 13c) become less steep and more convex, whereas the distal flank χ profiles (Figure 13d) do not appear to substantially change in response to advection.

During the uplift gradient and uplift gradient with advection phases of the modeling, we observe χ profiles indicative of drainage area loss on the proximal flank (Figure 13c), and drainage area gain on the distal flank (Figure 13d), as theorized in Figure 4c.

4.3. Drainage Patterns

4.3.1. Spacing Ratio

From a visual inspection of the drainage networks (Figure 5), it appears the dendritic drainage patterns observed during the uniform uplift and uplift gradient phases of the modeling are replaced by more elongate networks on both flanks but particularly on the proximal flank once advection is induced.

The spacing ratio is higher on the distal flank during the uplift gradient phase of the modeling, and higher on the proximal flank during the uplift gradient with advection phase of the modeling (Figure 12). This is observed in all simulations, although the difference in spacing ratio between the two flanks decreases with increasing fault dip angle; the spacing ratio is the same for both flanks ($=3.0$) when advection rate = 0.2 mm yr^{-1} and uplift rate at the fault = 0.5 mm yr^{-1} (Figure 12a).

For a given uplift gradient, faster advection is shown to produce higher spacing ratios on both flanks (Figure 12b). The magnitude of the uplift gradient is not shown to significantly affect the spacing ratio during the uplift gradient phase of the modeling; however higher spacing ratios are observed for the distal flank as the magnitude of the uplift gradient increases once advection is induced (Figure 12a).

The Sierra la Laguna exhibits a mean channel outlet spacing of 5.1 km on the proximal flank and 5.0 km on the distal flank, with a mean proximal and distal flank width value of 14.2 and 10.0 km respectively. This means the spacing ratio for the proximal and distal flanks of the Sierra la Laguna are 2.8 and 2.0 respectively.

4.4. Channel Characteristics

4.4.1. Longitudinal Profiles and χ Profiles

Channel longitudinal and χ profiles are presented for the numerical model where uplift gradient and advection are set to 0.2 mm yr^{-1} and wedge width is 25 km, corresponding to stage 3 of the numerical modeling setup. The observations presented here are representative of all model simulations.

Matching the observations from the mountain range cross-sections (Figure 6), channel longitudinal profiles on the proximal flank steepen in response to the uplift gradient (Figure 13a), whilst distal flank profiles become less steep (Figure 13b). Once advection is induced, proximal flank profiles become more linear and follow less of a concave up profile except toward the tops of channels (Figure 13a), whereas distal flank profiles become overall shorter and steeper again, in particular in their upper half (Figure 13b).

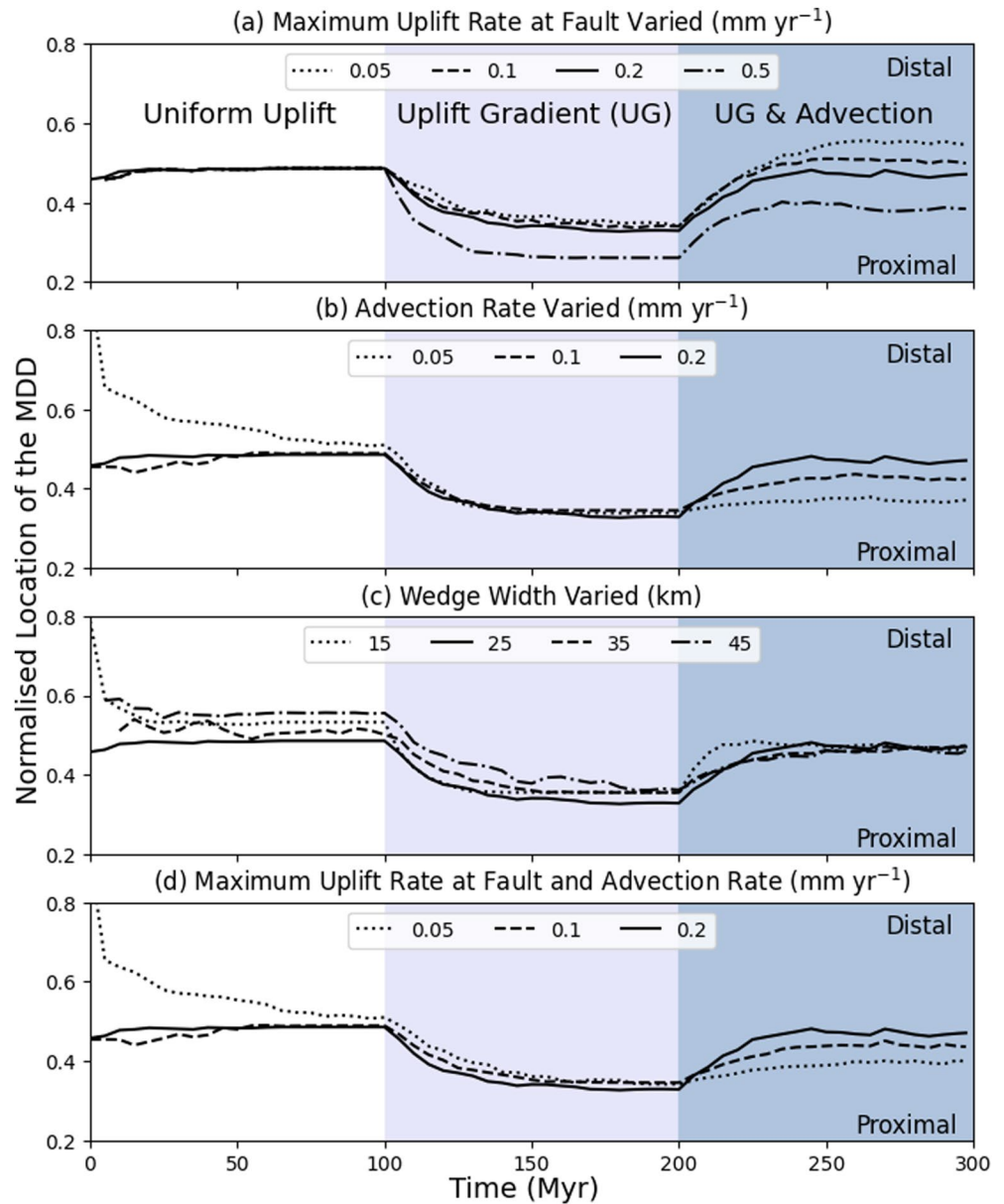


Figure 9. Normalized location of the Main Drainage Divide (MDD) as: (a) maximum uplift rate at the fault is varied (0.05, 0.1, 0.2, 0.5 mm yr⁻¹), (b) advection rate is varied (0.05, 0.1, 0.2 mm yr⁻¹), (c) wedge width is varied (15, 25, 35, 45 km), and (d) various maximum uplift rates at the fault alongside advection rates are set to represent normal faults with a dip angle of 45° (0.05, 0.1, 0.2 mm yr⁻¹). Each of these relates to a tectonic velocity (0.07, 0.14, 0.28 mm yr⁻¹ respectively), uplift and advection combined, that is observed at the fault. When not being varied, maximum uplift rate at the fault is set to 0.2 mm yr⁻¹, advection rate is set to 0.2 mm yr⁻¹, and wedge width is set to 25 km. Normalized MDD locations values can vary between 0 (proximal flank mountain front) and 1 (distal flank mountain front). The normalized location of the MDD is calculated every 5 Myr for the duration of each model run: 0–100 Myr uniform uplift of 0.1 mm yr⁻¹ (white); 100–200 Myr linear uplift gradient (lavender); 200–300 Myr same linear uplift gradient with the addition of advection (light blue).

Trunk channel longitudinal and χ profiles for the Sierra la Laguna are shown in Figure 14. Longitudinal profiles on the proximal flank (Figure 14a) are a combination of concave up profiles and profiles with a break in slope, reflecting a knickpoint with substantially reduced channel steepness toward channel headwaters. We can see these knickpoints more clearly in the χ profiles (Figure 14c), where these profiles become less steep upstream, reflecting a reduction in k_{sn} upstream. The proximal χ profiles are all convex, as seen in the modeling results. However, the convexity is much more pronounced in the natural landscape, with many prominent knickpoints.

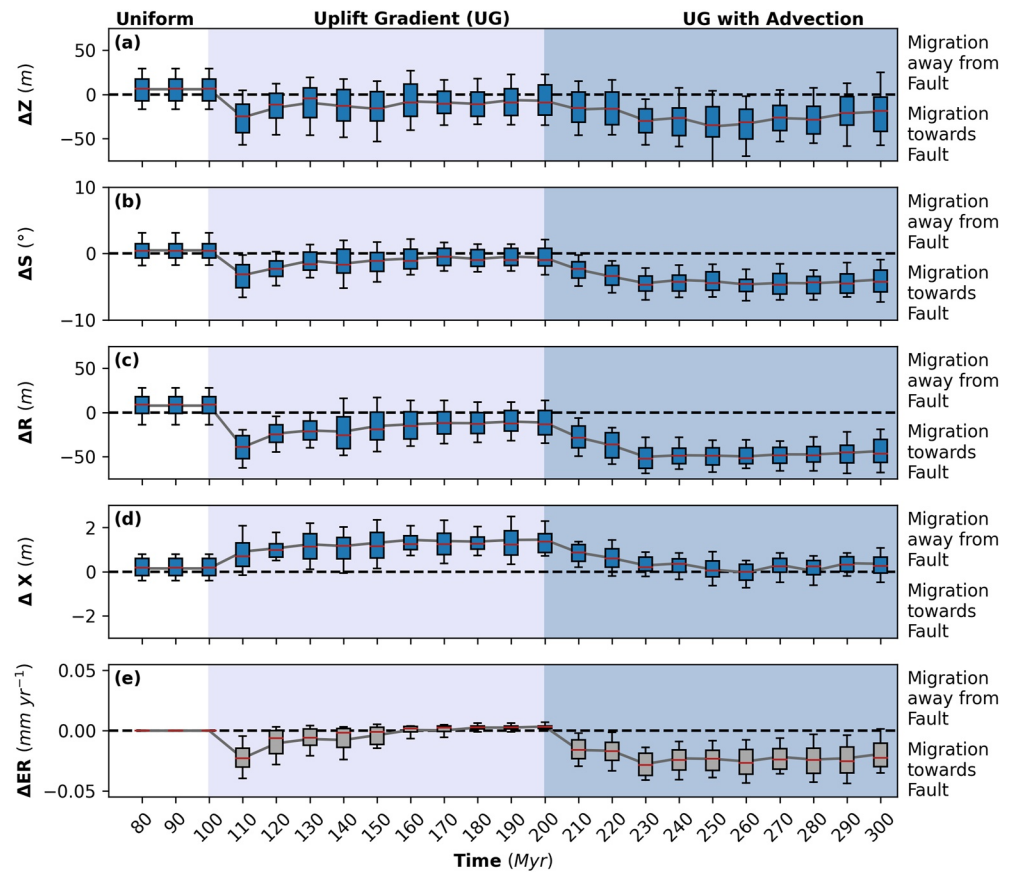


Figure 10. Across-Main Drainage Divide (MDD) Headwater Gilbert metric and χ Comparisons for: (a) ΔZ (Elevation), (b) ΔS (Slope), (c) ΔR (Relief), (d) $\Delta\chi$, and (e) ΔER (Erosion Rate). Positive and negative ΔZ , ΔS , ΔR , and $\Delta\chi$ values are expected to reflect higher erosion rates (ER) in proximal and distal flank headwaters, respectively. (e) Reflects observed across-MDD headwater differences in erosion rates (ΔER). Across-MDD Gilbert metric comparisons are calculated every 10 Myr between 80 and 300 Myr. 0–100 Myr uniform uplift of 0.1 mm yr^{-1} (white); 100–200 Myr linear uplift gradient with a maximum uplift rate at the fault of 0.2 mm yr^{-1} (lavender); 200–300 Myr same linear uplift gradient with the addition of advection at 0.2 mm yr^{-1} (light blue). Center line of the box plots (red) represents the median, the edges of the box relate to the 25th and 75th percentiles, and the whisker edges relate to the 10th and 90th percentiles. These results relate to model 3 in Table 1.

Conversely, longitudinal and χ profiles on the distal flank (Figures 14b and 14d) demonstrate the opposite. Longitudinal profiles display knickpoints at low elevation. Upstream of these knickpoints, the channel longitudinal profiles are concave up. We can also see these knickpoints in the χ profiles, where these profiles become steeper upstream, reflecting an increase in k_{sn} upstream. Note however that many of these χ profiles also show less steep segments at their head.

4.4.2. Normalized Channel Steepness

Distributions of normalized channel steepness (k_{sn}) values are shown in Figure 15 for a series of simulated mountain ranges, where the magnitude of the uplift gradient or the rate of advection has been varied.

k_{sn} is consistently higher on the proximal flank across all models (Figure 15). k_{sn} is observed to increase on both flanks as the magnitude of the uplift gradient increases (Figure 15a), whilst k_{sn} is observed to slightly but consistently decrease on both flanks as advection rate is increased (Figure 15b).

k_{sn} values for the Sierra la Laguna are shown in Figure 16. Generally, k_{sn} is higher on the proximal flank (Figure 16), although the contrast is not as strong as in the modeling results. We note that the k_{sn} values seem to taper toward the northern and southern tips of the fault-bounded range (Figure 16a).

This analysis was also carried out using only the trunk channels the model runs (Figure S1 in Supporting Information S1) and the Sierra la Laguna (Figure S2 in Supporting Information S1), to assess the impact tributaries flowing oblique to the uplift gradient may have on the distributions of k_{sn} (see Supporting Information S1). The

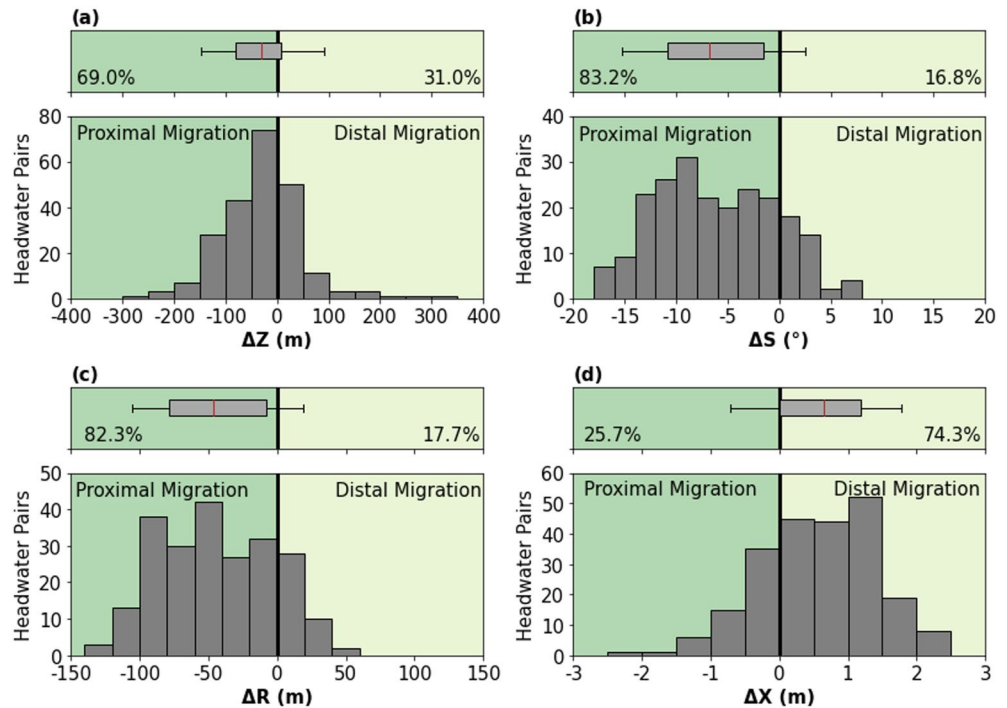


Figure 11. Histogram and box plot distributions for (a) ΔZ , (b) ΔS , (c) ΔR , and (d) $\Delta \chi$ across the Main Drainage Divide (MDD) for the Sierra la Laguna. Positive (light green) and negative (dark green) values are expected to indicate higher erosion rates in the proximal and distal flank headwaters, respectively, and therefore lead to migration of the MDD in a distal or proximal direction, respectively. Center line of the box plots (red) represents the median, the edges relate to the 25th and 75th percentiles, and the whiskers relate to the 5th and 95th percentiles.

results show greater contrasts in k_{sn} between flanks and narrower interquartile ranges, but the overall trends remain the same.

4.4.3. Channel Concavity

Channel concavity (θ) values derived from slope-area and χ -based methods are displayed in Figure 17. The slope-area θ provides an estimate of the apparent channel concavity, whilst the χ -derived θ using the disorder method should provide a value closer to the correct theoretical value (m/n exponent in the SPIM, Equation 4) (Mudd et al., 2018). As m/n is defined within the model's input ($m/n = 0.5$ in our case), these results are used to assess the impact of an uplift gradient and advection on the ability of such analyses to recover the correct theoretical values.

The θ values derived from slope-area and χ -based methods exhibit opposing patterns when comparing θ values between flanks in the modeled topographies (Figure 17). While the apparent θ from slope-area-based methods is higher on the distal flank (Figures 17c and 17d), as expected, χ -based methods suggest the opposite (Figures 17a and 17b). Slope-area-based methods suggest θ decreases on both flanks as the maximum uplift at the fault increases (Figure 17c), but no pattern is observed in relation to the advection rate (Figure 17d). The θ value derived from χ -based methods is not affected by the uplift (Figure 17a), or advection rate (Figure 17b).

The pattern of concavity indices across the divide in the Sierra la Laguna (Figure 18) is similar to those extracted from the numerical models (Figure 17), although the patterns in the Sierra la Laguna are not as pronounced as in the numerical models. In the Sierra la Laguna, χ -based methods suggest θ is higher on the proximal flank (Figure 18a), as in the modeling (Figures 17a and 17b), whilst slope-area-based methods suggest θ is similar on both flanks (Figure 18b). The θ values are also lower than in the modeling results, with central values around 0.35.

5. Discussion

The numerical modeling approach applied here allows us to demonstrate that advection alters mountain range dynamics, surface drainage patterns, and channel characteristics. Advection is also found to induce a continuous reorganization of drainage networks as a result of advective tectonic velocity.

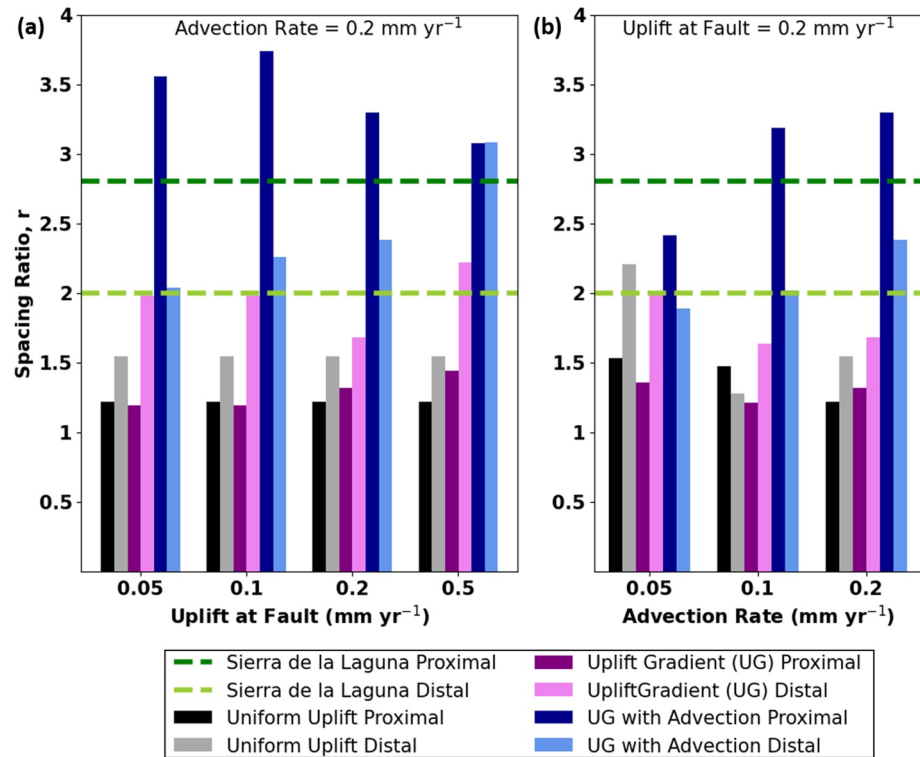


Figure 12. Spacing Ratio for the proximal and distal flanks at the end of each stage of uplift (Uniform uplift, Uplift Gradient, and Uplift Gradient with Advection), as (a) the uplift gradient is varied, and (b) the advection rate is varied. In essence, the different scenarios reflect differences in fault dip angle: when the maximum uplift rate at the fault increases for a given advection rate (a), the fault is getting steeper; when the advection rate increases for a given uplift rate at the fault (b), the fault dip angle decreases. The fault dip angle is 45° when advection rate = uplift rate at the fault. Note that the advection rate only affects the results of the “Uplift Gradient with Advection” scenarios (blue bars). Spacing Ratio for the proximal (dark green) and distal (light green) flanks of the Sierra la Laguna are also shown as dashed lines.

5.1. Mountain Range Dynamics

Advection creates an asymmetry distinct from that induced through an uplift gradient alone (Figure 6), with swath profiles taking a characteristic near linear shape on the proximal flank beyond the mountain front and a steep distal flank near the MDD. These observations are in agreement with earlier work investigating the influence of uplift gradients (Forte & Whipple, 2018; He et al., 2021; Whipple, Forte, et al., 2017; Zhou et al., 2022) and advection (Miller et al., 2007; Willett, 1999; Willett & Brandon, 2002; Willett et al., 2001) on mountain range (a)symmetry.

We interpret the asymmetry induced through advection as a geometrical change in the mountain range that is required to maintain a balance between the tectonic displacement (uplift and advection) and erosion. This is consistent with the theory that a mountain range will establish a spatial disequilibrium between uplift and erosion so as to account for the advective component of the tectonic forcing (Willett et al., 2001). We can observe this spatial disequilibrium in uplift and erosion rates in Figures 8e and 8f, where $U > E$ on the proximal flank and $U < E$ on the distal flank, facilitating growth on the proximal flank as material is advected headward, and decay on the distal flank as material is advected toward the distal mountain front.

We can also consider this as a geometrical problem where a point is advected along the mountain range's cross-section, from the proximal mountain front to the distal mountain front. In order for a mountain range experiencing advection to achieve a steady-state, the difference in elevation between the point's current location and where it will be after a period of tectonic displacement (the sum of motion from consecutive earthquakes) must be obtained through a spatial disequilibrium in uplift and erosion rates (Figure 19). For example, on the proximal flank, in order to increase the elevation of a point as it is advected toward the MDD, U must be greater than E . Similarly on the distal flank, in order to decrease the elevation of a point as it is advected toward the distal flank

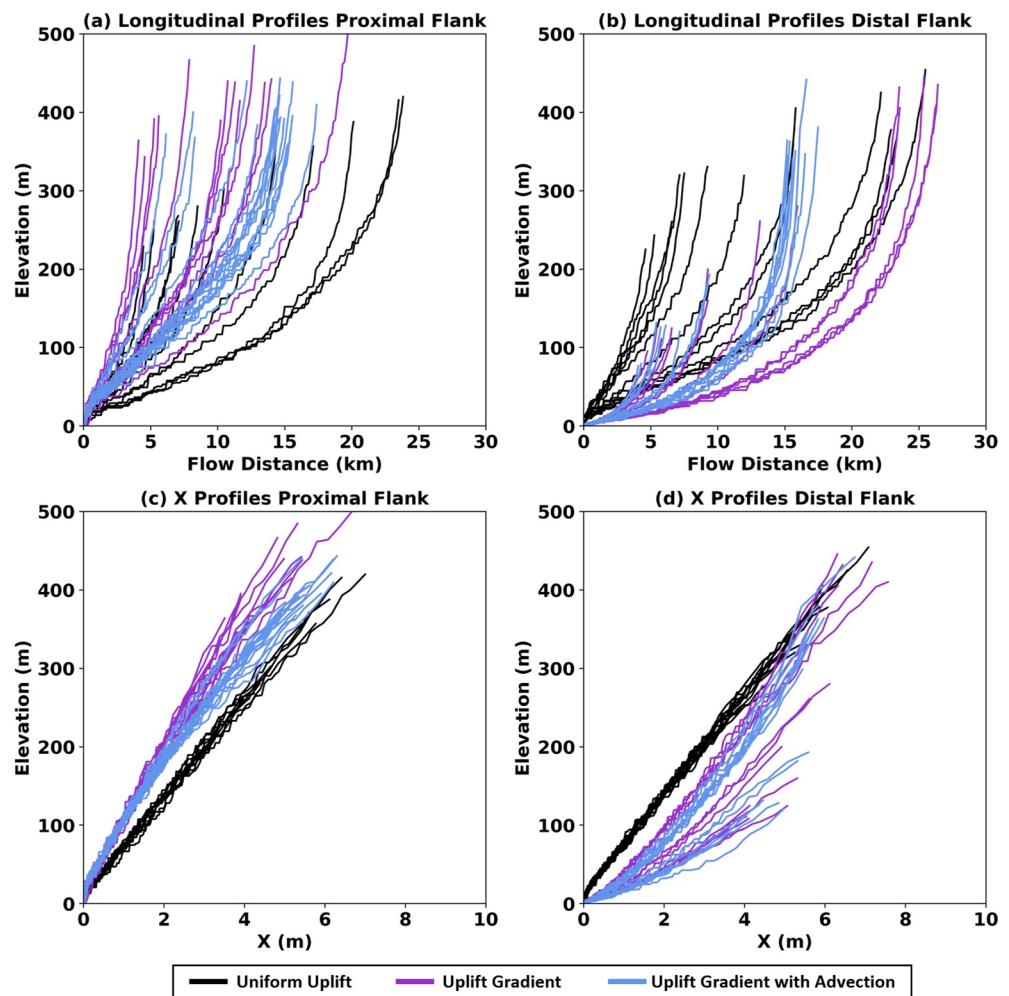


Figure 13. Modeled trunk channel longitudinal profiles for the: (a) proximal, and (b) distal, flanks of the simulated mountain range. Modeled trunk channel χ profiles for the: (c) proximal, and (d) distal, flanks of the simulated mountain range. Longitudinal and χ profiles are plotted for near steady-state landscapes given uniform uplift at 100 Myr (black), an uplift gradient at 200 Myr (purple), and an uplift gradient with advection at 300 Myr (violet). These profiles are extracted from the model where both the uplift gradient and the rate of advection are set to 0.2 mm yr⁻¹ and the wedge width is 25 km.

mountain front, U must be less than E . We consider this to be the main reason as to why we see this unequal balance between uplift rate and erosion rate during the advection scenario of the modeling (Figures 8c and 8f).

We also see that the magnitude of the uplift gradient and advection alters the normalized location of the MDD (Figure 9), where the MDD preferentially moves toward and away from the normal fault, when an uplift gradient and advection are induced, respectively. Again, this is in agreement with earlier work investigating the influence of uplift gradients (Forte & Whipple, 2018; Whipple, Forte, et al., 2017) and advection (He et al., 2021; Shi et al., 2021) on divide migration. Our modeling demonstrates that it is ultimately a combination of uplift gradient magnitude and advection rate that sets the stable location of the MDD (Figure 9).

When increasing the total tectonic velocity experienced by the fault, whilst maintaining the same fault dip angle by keeping the uplift and advection components of the tectonic velocity at the fault the same (Figure 9d), we see that advection exerts a stronger control over MDD location than the uplift gradient. We suggest advection exerts a stronger control in this scenario as it leads to more material being introduced into the mountain range system over a given amount of time, leading to greater relief, increasing steepness overall and producing greater differences in erosion rates across the MDD (Miller et al., 2007). This demonstrates that a change in the tectonic velocity can also result in a change in mountain range symmetry, surface drainage patterns and topographic characteristics. We note here however, that the fault dip angle will also exert a control over the relative importance of advection and uplift as tectonic velocity is varied.

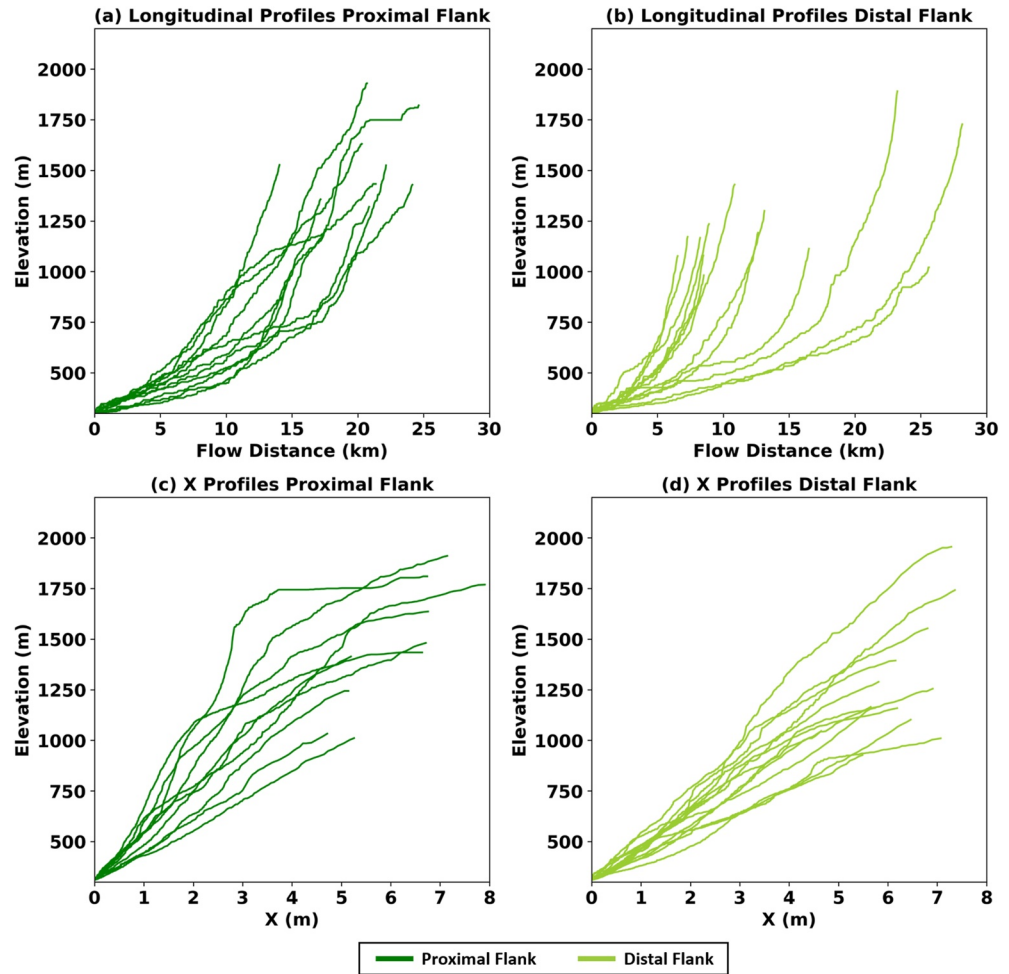


Figure 14. Channel longitudinal profiles for trunk channels on the: (a) proximal, and (b) distal, flanks of the Sierra la Laguna. Channel χ profiles for the trunk channels on the: (c) proximal, and (d) distal, flanks of the Sierra la Laguna. Proximal and distal flank profiles are shown in dark and light green respectively.

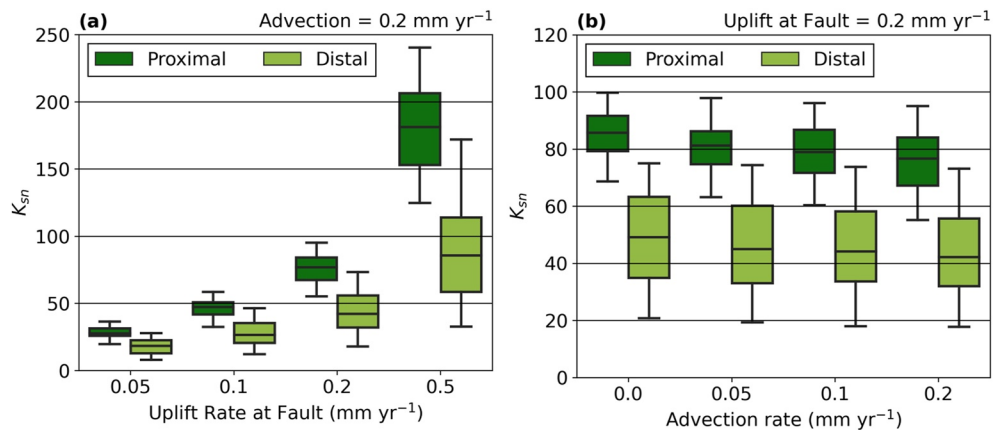


Figure 15. Normalized channel steepness (k_{sn}) distributions for modeled topographies as (a) the maximum uplift rate at the fault, and (b) the advection rate, is varied. k_{sn} distributions are given for both the proximal (dark green) and distal (light green) flanks. When the uplift gradient is being varied, advection rate is set to 0.2 mm yr^{-1} and when advection rate is being varied, the uplift gradient is set to 0.2 mm yr^{-1} . The center of the box plots represents the median, the edges of the box relate to the 25th and 75th percentiles, and the whisker edges relate to the 5th and 95th percentiles.

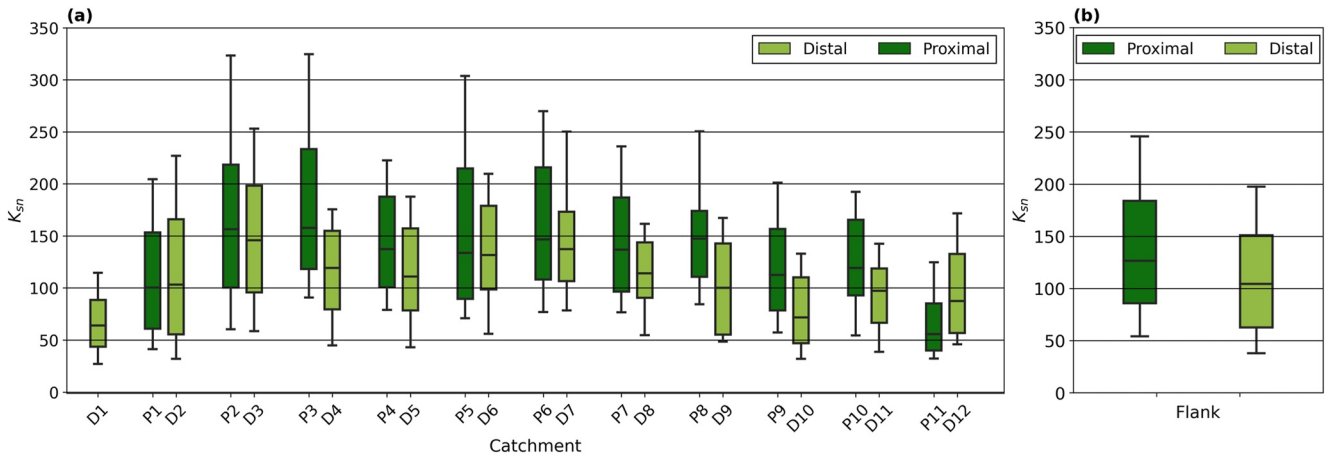


Figure 16. Normalized channel steepness (k_{sn}) distributions for the Sierra la Laguna by (a) catchment, and (b) flank. Catchments are labeled by flank (Proximal, P ; or Distal, D) and numbered north to south. k_{sn} distributions are given for both the proximal (dark green) and distal (light green) flanks. The center of the box plots represents the median, the edges of the box relate to the 25th and 75th percentiles, and the whisker edges relate to the 10th and 90th percentiles.

At the end of each phase of the numerical modeling, the normalized location of the MDD stabilizes (Figure 9). Across-MDD headwater Gilbert metric comparisons, ΔZ , ΔS , and ΔR (Figures 10a–10c), suggest across-MDD erosion rates return to similar values on each side of the divide at the end of the uplift gradient phase, with ΔZ , ΔS , and ΔR values returning to near 0. This pattern of erosion rates is observed within the numerical models (Figure 10e). However, ΔZ , ΔS , and ΔR values remain strongly negative at the end of the advection phase,

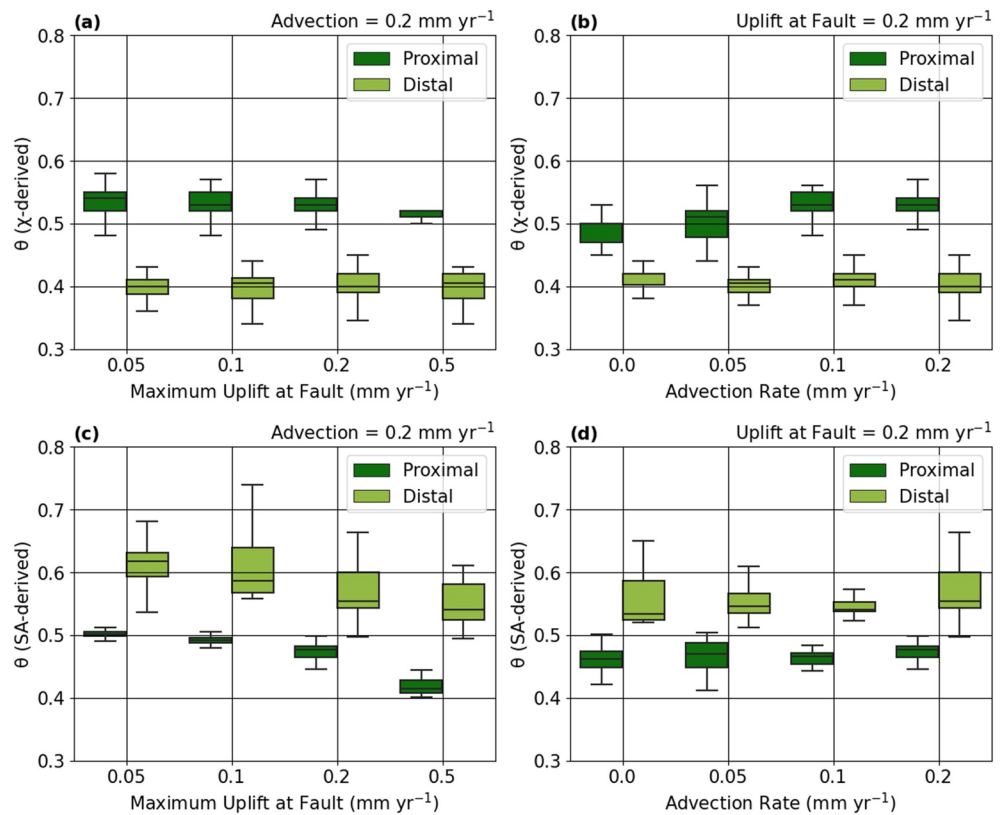


Figure 17. Box plots of the channel concavity index (θ) as (a, c) the maximum uplift rate at the fault is varied and (b, d) the advection rate is varied. θ is calculated using the χ -based method in (a, b) and using the slope-area-based method in (c, d). θ distributions are given for both the proximal (dark green) and distal (light green) flanks. When the uplift gradient is being varied, advection rate is set at 0.2 mm yr^{-1} and when advection rate is being varied, the uplift gradient is set at 0.2 mm yr^{-1} .

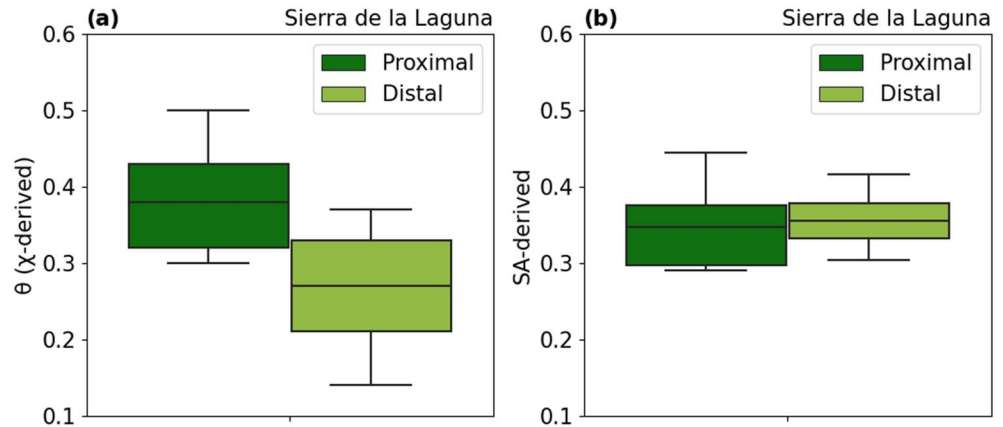


Figure 18. Box plots of the channel concavity index (θ) for the Sierra la Laguna, calculated using (a) the χ -based method, and (b) the slope-area-based method. θ distributions are given for both the proximal (dark green) and distal (light green) flanks.

suggesting consistently higher erosion rates in distal flank headwaters relative to the proximal flank headwaters (Figures 10a–10c). Again, this pattern of erosion rates is observed within the numerical models (Figure 10e). This disequilibrium persists even after the normalized location of the MDD has stabilized.

We attribute the incorrect prediction from the across-MDD χ metric ($\Delta\chi$), which reflects a migration of the MDD away from the fault during the uplift gradient and stabilization of the MDD during the uplift gradient with advection phase of the modeling (Figures 10d, 13c, and 13d), to a breach of the assumptions required for analysis of across-divide χ disequilibrium. Ideally, such analysis requires uniform lithology, uniform uplift, river systems sharing the same base-level and the absence of zones of active deposition and/or subsidence, as the χ value at the

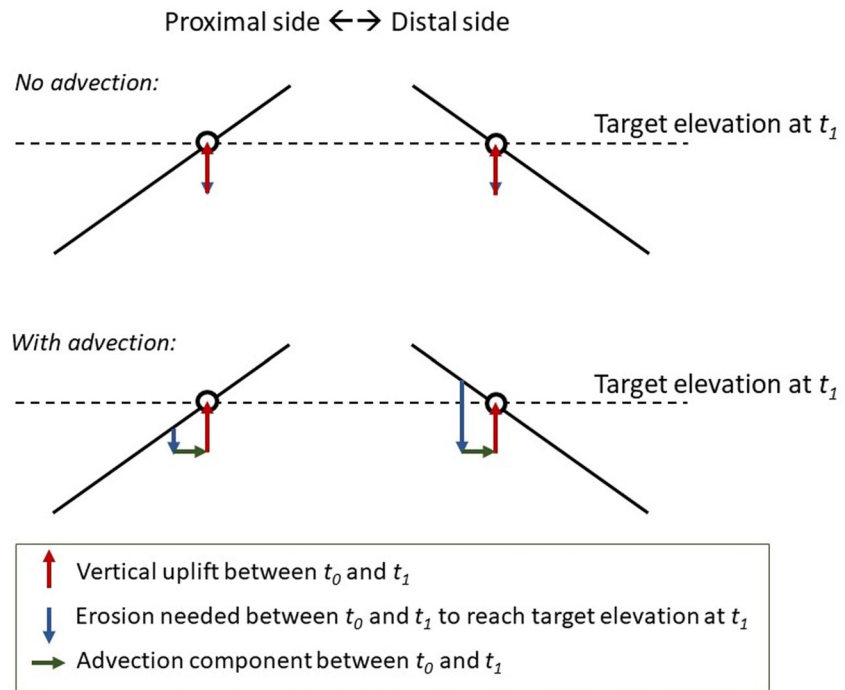


Figure 19. Simple geometrical explanation for erosional disequilibrium observed in the advection case (Figures 8e and 8f). With no advection (top), the vertical erosion rate needs to match the vertical uplift rate to preserve the steady-state topography. In the advection case (bottom), less erosion is needed for slopes facing toward the fault, and more erosion is needed for slopes facing away from the fault, to preserve the steady-state topography, using the fault as a reference.

divide will be a function of the steepness of the channel from its base-level to the divide (Perron & Royden, 2013; Whipple, Forte, et al., 2017). In our model, the only assumption that is breached is the fact that the uplift is non-uniform; our results therefore highlight the sensitivity of this metric to non-uniform uplift and therefore its limitation in determining drainage reorganization, especially in actively uplifting landscapes where uplift is unlikely to be uniform, such as in normal fault bounded mountain ranges. In the Sierra la Laguna, an additional assumption is breached, as using the same base-level (300 m) for both distal and proximal catchments (the sea) would lead to the inclusion of alluvial reaches on the distal side downstream of the fault. The distal mountain front is not clearly delineated and likely at an elevation different to the proximal mountain front. These reasons may explain why $\Delta\chi$ values in the Sierra la Laguna are consistent with neither the expectations from theory nor with the modeling results (Figures 10e and 11).

We interpret the combination of a stabilization in the normalized location of the MDD relative to the fault (Figure 9), and the occurrence of higher erosion rates in the headwaters of the distal flank relative to the proximal flank (Figure 10) as an indication that advection is being balanced by divide migration. The location of the MDD relative to the fault remains the same, however as new material surfaces at the fault from beneath the hanging wall (as simulated through moving the window of uplift, Section 3.1), the MDD is migrating into the uplifted wedge of material at the same rate as advection (Movie S1).

This suggests differences in erosion rates across the MDD exist to overcome advection which acts to move topography, geomorphic features, and material deemed immobile through fluvial processes from one side of the divide (proximal flank) to the other (distal flank) (Willett et al., 2001). The rate of divide migration must equate the rate of advection in order for the divide to remain spatially fixed relative to the fault. We therefore interpret this signal of divide migration across the MDD as an intrinsic mechanism that operates to balance the advective component of tectonic velocity. We may consider an analogy of this behavior in the form of a standing wave in a river, where the crest of a standing wave remains spatially fixed whilst water is transferred through the wave. In our mountain range, the crest of the wave is the MDD and the water being transferred is the footwall of the normal fault being advected through the mountain range (Movie S1).

This means divide migration and drainage reorganizations become a key mechanism through which mountain ranges experiencing a high component of tectonic advection can achieve steady-state. Consequently, we should expect to see evidence of strong across-divide disequilibrium, divide migration and drainage reorganization in mountain ranges with significant advective components (Willett et al., 2001).

5.2. Mountain Range Surface Drainage Patterns

A brief visualization of the numerically modeled landscapes (Figure 5) demonstrates significant reorganization of surface drainage networks in response to advection. Proximal and distal flank catchments lose their previous more dendritic drainage patterns and become far more elongate when advection is induced in phase 3 of the modeling (Figure 5 and Movie S1). In each of the model runs, we observe an increase in the spacing ratio (r) for both proximal and distal flank catchments when advection is induced (Figure 12), meaning catchments become substantially more elongate under the influence of advection.

Hovius (1996) suggests most linear mountain belts exhibit an r value of between 1.9 and 2.2. The r values we obtain during the advection phase of the modeling exceed this range with r values > 3 at advection rates $> 0.1 \text{ mm yr}^{-1}$. It has previously been suggested the distance between the mountain front and the MDD controls drainage outlet spacing (Attal, 2009; Bonnet, 2009; Giachetta et al., 2014; Hovius, 1996; Perron et al., 2009; Talling et al., 1997), meaning catchments and drainages are expected to reorganize in response to a change in flank width so as to maintain an optimal r value. However, the modeling presented here suggests the influence of tectonic forcings, particularly horizontal advection, may be more significant in determining outlet spacing, and in turn r , than originally thought.

Several mechanisms have been identified that operate to maintain an optimal r value as flank width changes, such as in response to a migrating MDD. These mechanisms can be separated into flank shortening and flank lengthening mechanisms. The flank shortening mechanisms include: splitting of drainage networks into two or more discrete catchments through drainage capture and diversion as originally demonstrated by Bonnet (2009); and across interfluvial competition as hypothesized by Talling et al. (1997) and demonstrated by Giachetta et al. (2014), where larger shrinking catchments, in contact with the MDD, lose area to smaller growing catchments that

previously formed triangular facet. along the mountain front. Flank lengthening mechanisms are currently limited to across interfluvial competition, where smaller catchments are encroached upon by larger adjacent catchments (Giachetta et al., 2014).

The numerical modeling presented here provides two new insights related to flank drainage reorganizations affecting r in response to advection. First, when the proximal flank lengthens in response to advection, instead of outlet spacing increasing as may be expected to maintain an optimal r value (Giachetta et al., 2014; Hovius, 1996; Perron & Royden, 2013; Talling et al., 1997), we observe a reduction in outlet spacing as triangular facets grow headwards into the mountain range interior until they eventually adjoin the MDD (Movie S1). This is different from the triangular facet growth hypothesized by Talling et al. (1997) and demonstrated by Giachetta et al. (2014), as this process occurs on a lengthening rather than shortening flank, and facilitates an increase in r value beyond the optimal range.

Second, we observe that when advection is induced, the distal flank shortens and outlet spacing decreases. However, instead of competition between adjacent catchments being the dominant mechanism altering outlet spacing, we see instead that catchments are split when a river's confluence is advected beyond the mountain front (Movie S1). As far as we are aware, this is a newly identified mechanism through which surface drainage patterns may respond to changes in tectonic forcings.

5.3. Channel Characteristics at the Mountain Range Scale

We analyzed the channel characteristics to determine if the channel profiles can be used to infer advection within a landscape. We observe that channel long profiles adjust substantially when advection is induced (Figure 13), largely reflecting changes in flank widths. These changes alter the normalized channel steepness (k_{sn}) of the channels. We find k_{sn} is greater on the proximal flank in all model runs, reflecting the uplift gradient (Figure 15). We also find that the faster the advection rate, the lower k_{sn} is on both flanks (Figure 15b). We suggest this reduction in k_{sn} at faster advection rates results from a reduction in the total uplift experienced by any point in the landscape, as faster advection rates will move any singular point in the landscape away from areas of faster uplift more quickly. In addition, advection itself has previously been associated with a reduced channel steepness (in the absence of an uplift gradient): displacement on a fault with a lower dip angle (and therefore a greater advection component) will lead to a reduction in the flux of material uplifted with respect to a reference elevation, meaning the greater the advection rate the lower the erosion rate needed to counterbalance the uplift (Miller et al., 2007). We suggest a combination of these factors result in channels needing to incise less and this is reflected in reduced k_{sn} at faster advection rates.

The modeling shows a reduction in k_{sn} toward the headwaters of the proximal flank, and the opposite on the distal flank, in both uplift gradient and uplift gradient with advection scenarios (Figures 13c and 13d). The reduction in k_{sn} toward the headwaters of the proximal flank is more prominent with advection compared to the uplift gradient only scenario, but the difference is likely not strong enough to allow us to discriminate between the two scenarios in nature. This pattern in the χ plots is indicative of a drainage migration toward the fault (Willett et al., 2014; Yang et al., 2015), as illustrated in Figure 4c, where an increase and decrease in k_{sn} toward the headwaters is indicative of area loss and gain, respectively (Willett et al., 2014; Yang et al., 2015).

The most distinctive feature of advection appears to be the observed imbalance in across-MDD erosion rates as predicted through the Gilbert metrics (Figure 10) while the MDD remains spatially fixed relative to the fault. Both Gilbert metrics and shape of profiles in χ plots exhibit features that are frequently considered representative of divide migration, yet we know the MDD is not migrating with respect to the fault. Instead, the advected topography is being "passed through" the MDD which has to effectively migrate toward the fault to overcome the effect of advection that pushes it away from the fault (Movie S1). We can summarize this by saying that, in order for any feature to maintain a fixed position in the landscape, that feature must have a rate of migration equal and opposite to the rate of advection. Whether a divide can migrate at the rate of advection will depend on numerous factors including the erodability of the substrate (K), hillslope diffusivity (D), and the channel concavity (θ) as set by the ratio between m and n (Whipple, Forte, et al., 2017). Note the fact that contrasts in erosion rates are better reflected in the Gilbert metrics than in the river profiles is consistent with the suggestion by Miller et al. (2007), that "the least ambiguous evidence for lateral advection (...) is expected to occur on hillslopes and in colluvial valleys because their steep slopes and short length scales make their morphologies less complicated by gradients

in rock uplift rate or changes in lithology.” Indeed, the difference in uplift rate between the hillslopes that the Gilbert metrics analyses focus on in the vicinity of the MDD is expected to be minimal.

As the m/n ratio, and therefore the theoretical value of θ , is 0.5 in our model simulations, any variance from this value can be interpreted as a feature of the tectonic forcings we place on the landscape. We see that an uplift gradient with no advection perturbs θ and that the addition of advection only has a minimal effect on θ (Figures 17b and 17d). We also see that the χ and Slope-Area approaches to extracting θ produce consistently opposite outcomes, with higher θ observed on the proximal flank for the χ approach, and higher θ observed on the distal flank for the slope-area approach. In all modeled cases, the values on both sides of the mountain range bracket the actual value of 0.5 set in the model. The results conform to the expectation of a more and less concave distal and proximal flank, respectively, using the Slope-Area approach, as observed in earlier studies of uniform uplift (Miller et al., 2007). This reflects spatial disequilibrium between uplift and erosion rates (Figure 8). The cause of the opposite trend using the χ approach is unknown, but is not a diagnostic feature of advection, as the same observations are made in the uplift gradient scenarios with and without advection (Figure 17).

5.4. Comparison With the Sierra La Laguna

The cross-section of the Sierra la Laguna (Figure 7a) displays a convex proximal flank and a concave distal flank, as observed in the numerical modeling when advection is included (Figure 6). When the Sierra la Laguna cross-section is plotted based on distance from the MDD (Figure 7b), we also see a faster reduction in elevation with distance from the MDD on the distal flank than on the proximal flank, something that is also observed in the numerical modeling, both during the uplift gradient only and uplift gradient with advection scenarios (Figure 6). This means the Sierra la Laguna's cross-section appears indicative of an uplift gradient. However, it is not possible to distinguish between the presence or absence of advection in the Sierra la Laguna based upon the cross-section alone.

The high spacing ratios (r) for the Sierra la Laguna (2.8 on the proximal and 2.0 on the distal flanks respectively) are comparable to that of the modeled topographies when an uplift gradient with advection is applied (Figure 12). The visibly highly elongate catchments on the proximal flank of the Sierra la Laguna (Figure 2) are also comparable to those forming in the numerical modeling when advection is induced (Figure 5). We suggest that highly elongate catchments on the proximal flank of fault-bounded mountain ranges are diagnostic of a high advective component in the tectonic velocity vector associated with displacement on the adjacent faults. Bot et al. (2016) proposed that “the parallel geometry of the eastern streams in continuity with the western streams by dry valleys was constrained by regularly spaced corrugations that formed on the convex footwall of a major detachment fault plane, either reflecting the presence of “megamullions” or folding in a transtensional context.” Our results offer an alternative explanation for the origin of the observed elongate catchments.

The convex nature of channels in the headwaters of the proximal flank in the Sierra la Laguna, when combined with field observations of beheaded channels and valleys that are wider than would be anticipated given present-day drainage areas (Bot et al., 2016), can be interpreted as evidence of drainage area loss in the headwaters of proximal flank catchments. This is further supported by headwater Gilbert metric comparisons across the MDD (Figure 11) that are indicative of slower erosion in proximal flank headwaters and faster erosion in distal flank headwaters. These observations clearly indicate migration of the MDD toward the fault. Differences in erosion rates across the MDD were also observed in the numerical modeling in both the uplift gradient only and uplift gradient with advection scenarios (Figure 10e). The Gilbert metrics reflected this difference in erosion rates well (Figures 10a–10c). The strength of the disequilibrium observed across the MDD of the Sierra la Laguna is comparable to that in the uplift gradient with advection modeling scenario, suggesting the MDD is actively migrating toward the fault to overcome the effect of advection on the low angle San José del Cabo normal Fault.

Overall we see that the channels draining the Sierra la Laguna are generally steeper on the proximal flank and less steep on the distal flank (Figures 14 and 16). This matches observations made in the numerical modeling during the uplift gradient only and uplift gradient with advection scenarios (Figures 13 and 15). The knickpoints in the headwaters of the profiles in χ plots, leading to overall convex profiles on the proximal side and concave profiles on the distal side, are also consistent with these modeling results, although the knickpoints are less systematic and more abrupt in the natural landscape compared to the modeled topographies (Figure 14). In a similar way to the cross-sectional analysis, however, we cannot differentiate between the absence or presence of advection

using the channel profiles alone. The same applies to the estimates of θ which are not significantly affected by advection. The χ -based approach provides θ values that are higher on the proximal side than on the distal side of the Sierra la Laguna, as observed in the modeled results in the uplift gradient and uplift gradient with advection scenarios. Surprisingly, the Slope-Area approach provides θ values that are low (≈ 0.35) and indistinguishable on both proximal and distal sides of the Sierra la Laguna. The presence of multiple prominent convexities in the river profiles may influence the results (Figure 14).

Two features that are common in the Sierra la Laguna, but are not found in the modeled topographies, are (a) low gradient, low relief areas in the headwaters of the proximal and distal catchments, and (b) the formation and preservation of windgaps along the MDD (Bot et al., 2016). The low gradient, low relief areas can be seen as flat reaches at the very top of some of the river profiles on both flanks (Figure 14). Windgaps are found where two catchments draining opposite flanks adjoin to form part of the MDD, and channels within these catchments meet the MDD at the same location, thereby creating a break in the ridgeline of the MDD. Miller and Slingerland (2006), show that windgaps can form when proximal flank topography, such as river valleys and ridges are advected across the MDD. This results in catchment beheading on the proximal flank and a transfer of relic valleys across the MDD to the distal flank, however drainage lines are not preserved in this form of drainage reorganization (Bishop, 1995). We suggest the windgaps found along the MDD of the Sierra la Laguna are an example of this.

These two features indicate that MDD migration can result from progressive migration but also from discrete capture events. In the latter case, upstream sections of the proximal catchments can become disconnected from their main stem (e.g., as a result of backtilting) and become vulnerable to capture by aggressive distal channels (Attal et al., 2008; Shelef & Goren, 2021). Channels on the proximal flank within the model do not have complex branching and this makes capture unlikely. In a natural setting, heterogeneities in lithology could also promote capture of proximal flank channels by distal flank headwaters: for example, Mitchell and Forte (2023) demonstrate that advection involving lithological contacts enhances drainage divide migration.

Cooling histories derived from thermochronology are characterized by constant cooling for the last 10–12 Myr at both the eastern (proximal) and western (distal) margins of the Los Cabos block (Fletcher et al., 2000). There is no evidence of recent tectonic change that could have driven the observed drainage reorganization in the Sierra la Laguna, although we recognize that histories derived from thermochronology do not have the granularity that could allow us to unambiguously dismiss a potential tectonic driver of disequilibrium. We can also dismiss potential climatic and lithological drivers of MDD migration in the Sierra la Laguna (Bot et al., 2016; Fletcher et al., 2000; Fletcher & Munguía, 2000; Garcillán et al., 2010). Therefore, the advective tectonic control that we have modeled here appears to be the most suitable explanation for drainage reorganization in the present-day Sierra la Laguna.

5.5. Limitations and Future Directions

The numerical modeling framework applied in this study helps to disentangle the effects of uplift and advection on topographic form. However, like all numerical models, the model is limited by its simplicity and ability to only reflect the processes and concepts built into them. As a detachment-limited model, there is no consideration given to the role of sediment in these simulated landscapes. We hypothesize that sediment is likely to lead to a feedback, whereby the deposition of sediment in low k_{sn} channels or in channels that have recently lost drainage area will reduce sediment mobility and promote a further reduction in k_{sn} and further drainage area loss. In the context of our study where advection moves features that cannot exert an opposite force to advection, it is likely that channels with abundant surplus material will be passively translated to the headwaters of the proximal flank. This material may be preserved in the landscape until it is advected past the MDD and removed by erosion in the distal flank catchments. This process could explain the presence of low gradient, low relief segments near the MDD, in the headwaters of both proximal and distal channels (demonstrating passive translation and recent integration, respectively). An assessment of the role of sediment in modulating topography and drainages in these landscapes would be useful to further develop our understanding of how advection affects mountain range dynamics, topography and drainage.

Divide migration is not just influenced by the tectonic forcings of uplift and advection. There are a range of parameters that will influence the stable location of a drainage divide, and the rate at which a divide is able

to migrate. These include; the erodability of the substrate (K), hillslope diffusivity (D), and channel concavity (θ) as set by the ratio of m to n (Whipple, Forte, et al., 2017). There will likely be landscapes where the rate of advection exceeds the achievable rate of divide migration, for example, where precipitation is very low. In these landscapes it is unlikely that an equilibrium between the rate of advection and the rate of divide migration will develop; instead we may anticipate the development of relic landscapes as outlined by Eizenhöfer et al. (2019).

One assumption that we have made in the modeling is that the rate of advection is constant and uniform throughout the landscape. It is possible that the rate of advection, like uplift, decreases with distance from the fault. Advection and uplift rates may also taper toward the tips of the fault (e.g., Cowie et al., 2006; Mudd, Roda-Boluda, et al., 2022), as suggested by the patterns of decreasing k_{sn} toward the northern and southern tips of the Sierra la Laguna (Figure 16). A reduction in the rate of advection with distance from and along the fault would impact the control exerted by advection in different parts of the mountain range and lead to more complex responses than observed.

To develop a clearer understanding of how landscapes respond to advection, a comprehensive study of the spatial distribution of erosion rates in a mountain range that is known to be experiencing advection would help to provide a basis upon which natural landscapes and numerical models can be compared in a way that does not rely purely on topographic observations.

This study has demonstrated that advection as a tectonic component, may be more significant in shaping mountain range topography and drainage patterns than previously thought. We recommend that advection should be excluded from modeling only in circumstances where the effects of advection can be clearly demonstrated to be negligible.

Finally, the topographic metrics (Gilbert and χ) that are commonly used to infer divide migration, whilst appropriate metrics for easily predicting differences in erosion rates across divides, may not necessarily give an accurate picture of the true spatial migration of the divide, depending on the reference frame used. We have demonstrated that Gilbert metrics and χ profiles can demonstrate across-divide differences in erosion rates when the divide remains spatially fixed with respect to a fault with a strong advection component. This occurs as the divide must establish an across-divide difference in erosion rates in order to migrate toward the fault at the same rate as it is being advected away from the fault. This is necessary for the landscape to achieve a dynamic steady-state. We caution against using these topographic metrics alone to infer a migration of a divide without giving consideration to the potential advective component of the tectonics in the studied landscape. Additionally, differences in Gilbert metrics or χ at a drainage divide are often used to label catchments as aggressor or victim, with the former growing at the expense of the latter. Victim catchments are expected to shrink. However, in a situation where a drainage divide is migrating toward a fault at a rate lower than the topography is advected away from the fault, the catchments that would be termed "victim catchments" through an across-MDD topographic analysis would actually be growing in drainage area, as the area gain at the mountain front through advection at the fault would be greater than the area lost at the MDD.

6. Conclusions

Our study has focused on identifying the relative influence of the vertical and horizontal components of tectonic displacement on the development of topography in a normal fault bound mountain range. The numerical modeling we have conducted independently tested the effects of uniform uplift, an uplift gradient, and an uplift gradient with advection. An uplift gradient induces a migration of the MDD toward the fault, whilst advection does the opposite. In the uniform uplift and uplift gradient scenarios, vertical uplift and vertical erosion are balanced ($U = E$) at all points across the mountain range. However, in the advection scenario, $U > E$ on the proximal flank, and $U < E$ on the distal flank. This erosion disequilibrium is a direct result of the horizontal displacement of topography through tectonic advection.

We have demonstrated that geomorphic features, such as drainage divides, may remain spatially fixed while experiencing tectonic advection, allowing the landscape to reach steady-state. They do so by developing a pattern of erosion rates that produces a migration of the geomorphic feature in the opposite direction to advection. This means faster erosion rates on the distal side and slower erosion rates on the proximal side. For any feature to remain spatially fixed in a landscape experiencing advection, that feature must have a rate of migration equal and opposite to the rate of advection. Consequently, divide migration does not necessarily equate to growth and

shrinkage of adjacent catchments and the influence of advection in a landscape should be considered before inferring a change in drainage area.

We have also identified two mechanisms through which advection driven drainage reorganization can alter channel and catchment spacing, although we recognize they require further investigation, as the modeled dynamic response to advection may be influenced by the type of numerical model used. First, a growth of triangular facets at the proximal mountain front into the mountain range interior, driven by advection stretching the facet. And, second, the splitting of channels as river confluences are advected beyond the distal mountain front. Each of these occurs where a geomorphic feature (the divide between the triangular facet and adjacent drainages, and the river confluence) is advected at a faster rate relative to the rate the feature is able to migrate at in the opposite direction to advection.

We have shown that faster advection acts to reduce k_{sn} across a mountain range. We have suggested this reduction in k_{sn} develops from reducing the total time that any given point in the landscapes experiences high uplift and in turn the total uplift experienced by any point in the landscape. This means channels can balance uplift with less steep channels.

Comparison of the modeled topographies with that of the Sierra la Laguna reveals strong similarities. The distinctive features that characterize a landscape's response to advection in our model are also observed in the natural landscape, thereby demonstrating the importance of advection in driving the evolution of the Sierra la Laguna. These features include: topographic evidence of MDD migration toward the fault (as identified from headwater Gilbert metric comparisons and beheaded channels on the proximal flank), highly elongated catchments on the proximal flank, and asymmetry in channel profile and mountain range cross section.

While we find the asymmetry (channel profile and mountain range) is not diagnostic of advection (as an uplift gradient alone will generate asymmetry), we believe that erosional disequilibrium at the MDD (as revealed by Gilbert metrics and χ profiles) and elongate catchments are illustrative of tectonic displacements with a high advective component, as consistently demonstrated in our numerical modeling and observations of the Sierra la Laguna.

Data Availability Statement

The datasets are stored in the following data repository: <https://doi.org/10.7488/ds/3809> (Hoskins et al., 2023).

Acknowledgments

This work is supported by a NERC Doctoral Training Partnership Grant (NE/S007407/1). We would like to thank H. Dow, S. Miller, an anonymous reviewer and the Associate Editor for thoughtful comments and feedback that have helped to improve the paper.

References

- Adams, B. A., Whipple, K. X., Forte, A. M., Heimsath, A. M., & Hodges, K. V. (2020). Climate controls on erosion in tectonically active landscapes. *Science Advances*, 6(42), 3166. <https://doi.org/10.1126/sciadv.aaz3166>
- Attal, M. (2009). Rivers split as mountains grow. *Nature Geoscience*, 2(11), 747–748. <https://doi.org/10.1038/ngeo675>
- Attal, M., Tucker, G. E., Whittaker, A. C., Cowie, P. A., & Roberts, G. P. (2008). Modeling fluvial incision and transient landscape evolution: Influence of dynamic channel adjustment. *Journal of Geophysical Research*, 113(F3), F03013. <https://doi.org/10.1029/2007JF000893>
- Beeson, H. W., McCoy, S. W., & Keen-Zebert, A. (2017). Geometric disequilibrium of river basins produces long-lived transient landscapes. *Earth and Planetary Science Letters*, 475, 34–43. <https://doi.org/10.1016/j.epsl.2017.07.010>
- Berlin, M. M., & Anderson, R. S. (2007). Modeling of knickpoint retreat on the roan plateau, western Colorado. *Journal of Geophysical Research*, 112(F3), F03S06. <https://doi.org/10.1029/2006JF000553>
- Bernard, T., Sinclair, H. D., Gailleton, B., & Fox, M. (2021). Formation of longitudinal river valleys and the fixing of drainage divides in response to exhumation of crystalline basement. *Geophysical Research Letters*, 48(8), e2020GL092210. <https://doi.org/10.1029/2020GL092210>
- Bishop, P. (1995). Drainage rearrangement by river capture, beheading and diversion. *Progress in Physical Geography: Earth and Environment*, 19(4), 449–473. <https://doi.org/10.1177/030913339501900402>
- Bonnet, S. (2009). Shrinking and splitting of drainage basins in orogenic landscapes from the migration of the main drainage divide. *Nature Geoscience*, 2(11), 766–771. <https://doi.org/10.1038/ngeo666>
- Bot, A., Geoffroy, L., Authemayou, C., Bellon, H., Graindorge, D., & Pik, R. (2016). Miocene detachment faulting predating EPR propagation: Southern Baja California: Miocene detachment, Baja California. *Tectonics*, 35(5), 1153–1176. <https://doi.org/10.1002/2015TC004030>
- Burrough, P. A., & McDonnell, R. A. (1998). *Principles of geographical information systems* (Vol. 190). Oxford University Press.
- Castelltort, S., Goren, L., Willett, S. D., Champagnac, J.-D., Herman, F., & Braun, J. (2012). River drainage patterns in the New Zealand Alps primarily controlled by plate tectonic strain. *Nature Geoscience*, 5(10), 744–748. <https://doi.org/10.1038/ngeo1582>
- Cowie, P. A., Attal, M., Tucker, G. E., Whittaker, A. C., Naylor, M., Ganas, A., & Roberts, G. P. (2006). Investigating the surface process response to fault interaction and linkage using a numerical modelling approach. *Basin Research*, 18(3), 231–266. <https://doi.org/10.1111/j.1365-2117.2006.00298.x>
- Douglass, J., & Schmeeckle, M. (2007). Analogue modeling of transverse drainage mechanisms. *Geomorphology*, 84(1–2), 22–43. <https://doi.org/10.1016/j.geomorph.2006.06.004>
- Duque-Trujillo, J., Ferrari, L., Orozco-Esquivel, T., López-Martínez, M., Lonsdale, P., Bryan, S. E., et al. (2015). Timing of rifting in the southern Gulf of California and its conjugate margins: Insights from the plutonic record. *Geological Society of America Bulletin*, 127(5–6), 702–736. <https://doi.org/10.1130/B31008.1>

- Eizenhöfer, P. R., McQuarrie, N., Shefel, E., & Ehlers, T. A. (2019). Landscape response to lateral advection in convergent orogens over geologic time scales. *Journal of Geophysical Research: Earth Surface*, 124(8), 2056–2078. <https://doi.org/10.1029/2019JF005100>
- Fletcher, J. M., Kohn, B. P., Foster, D. A., & Gleadow, A. J. W. (2000). Heterogeneous Neogene cooling and exhumation of the Los Cabos block, southern Baja California: Evidence from fission-track thermochronology. *Geology*, 28(2), 107–110. [https://doi.org/10.1130/0091-7613\(2000\)028<0107:hnaeco>2.3.co;2](https://doi.org/10.1130/0091-7613(2000)028<0107:hnaeco>2.3.co;2)
- Fletcher, J. M., & Munguía, L. (2000). Active continental rifting in southern Baja California, Mexico: Implications for plate motion partitioning and the transition to seafloor spreading in the Gulf of California. *Tectonics*, 19(6), 1107–1123. <https://doi.org/10.1029/1999TC001131>
- Forte, A. M., & Whipple, K. X. (2018). Criteria and tools for determining drainage divide stability. *Earth and Planetary Science Letters*, 493, 102–117. <https://doi.org/10.1016/j.epsl.2018.04.026>
- Gailleron, B., Mudd, S. M., Clubb, F. J., Grieve, S. W. D., & Hurst, M. D. (2021). Impact of changing concavity indices on channel steepness and divide migration metrics. *Journal of Geophysical Research: Earth Surface*, 126(10), e2020JF006060. <https://doi.org/10.1029/2020JF006060>
- Garcillán, P. P., Abraham, C. E. G., & Ezcurra, E. (2010). The cartographers of life: Two centuries of mapping the natural history of Baja California. *Journal of the Southwest*, 52(1), 1–40. <https://doi.org/10.1353/jsw.2010.0001>
- Giachetta, E., Refice, A., Capolongo, D., Gasparini, N. M., & Pazzaglia, F. J. (2014). Orogen-scale drainage network evolution and response to erodibility changes: Insights from numerical experiments. *Earth Surface Processes and Landforms*, 39(9), 1259–1268. <https://doi.org/10.1002/esp.3579>
- Gilbert, G. K. (1877). *Geology of the Henry Mountains (technical report)*. US: Government Printing Office: USGS.
- Guerit, L., Goren, L., Dominguez, S., Malavieille, J., & Castelltort, S. (2018). Landscape 'stress' and reorganization from -maps: Insights from experimental drainage networks in oblique collision setting: Landscape stress and reorganization from -maps. *Earth Surface Processes and Landforms*, 43(15), 3152–3163. <https://doi.org/10.1002/esp.4477>
- Hack, J. T. (1960). Interpretation of erosional topography in humid temperate regions. *American Journal of Science*, 258(A), 80–97.
- Harel, M. A., Mudd, S. M., & Attal, M. (2016). Global analysis of the stream power law parameters based on worldwide ¹⁰Be denudation rates. *Geomorphology*, 268, 184–196. <https://doi.org/10.1016/j.geomorph.2016.05.035>
- He, C., Yang, C.-J., Turowski, J. M., Rao, G., Roda-Boluda, D. C., & Yuan, X.-P. (2021). Constraining tectonic uplift and advection from the main drainage divide of a mountain belt. *Nature Communications*, 12(1), 544. <https://doi.org/10.1038/s41467-020-20748-2>
- Hilley, G. E., & Arrowsmith, J. R. (2008). Geomorphic response to uplift along the Dragon's Back pressure ridge, Carrizo Plain, California. *Geology*, 36(5), 367. <https://doi.org/10.1130/G24517A.1>
- Hoskins, A., Attal, M., Mudd, S., & Castillo, M. (2023). Topographic response to horizontal advection in Normal Fault-Bound Mountain Ranges [Dataset]. School of GeoSciences, University of Edinburgh. <https://doi.org/10.7488/ds/3809>
- Hovius, N. (1996). Regular spacing of drainage outlets from linear mountain belts. *Basin Research*, 8(1), 29–44. <https://doi.org/10.1111/j.1365-2117.1996.tb00113.x>
- Howard, A. D., Dietrich, W. E., & Seidl, M. A. (1994). Modeling fluvial erosion on regional to continental scales. *Journal of Geophysical Research*, 99(B7), 13971–13986. <https://doi.org/10.1029/94jg00744>
- Howard, A. D., & Kerby, G. (1983). Channel changes in badlands. *Geological Society of America Bulletin*, 94(6), 739. [https://doi.org/10.1130/0016-7606\(1983\)94\(739:CCIB\)2.0.CO;2](https://doi.org/10.1130/0016-7606(1983)94(739:CCIB)2.0.CO;2)
- Hurst, M. D., Mudd, S. M., Attal, M., & Hilley, G. (2013). Hillslopes record the growth and decay of landscapes. *Science*, 341(6148), 868–871. <https://doi.org/10.1126/science.1241791>
- Hurst, M. D., Mudd, S. M., Walcott, R., Attal, M., & Yoo, K. (2012). Using hilltop curvature to derive the spatial distribution of erosion rates. *Journal of Geophysical Research*, 117(F2), 2011JF002057. <https://doi.org/10.1029/2011JF002057>
- Hurst, M. D., Mudd, S. M., Yoo, K., Attal, M., & Walcott, R. (2013). Influence of lithology on hillslope morphology and response to tectonic forcing in the northern sierra Nevada of California. *Journal of Geophysical Research: Earth Surface*, 118(2), 832–851. <https://doi.org/10.1002/jgrf.20049>
- Kirby, E., & Whipple, K. (2001). Quantifying differential rock-uplift rates via stream profile analysis. *Geology*, 29(5), 415. [https://doi.org/10.1130/0091-7613\(2001\)029\(0415:QDRURV\)2.0.CO;2](https://doi.org/10.1130/0091-7613(2001)029(0415:QDRURV)2.0.CO;2)
- Lague, D. (2014). The stream power river incision model: Evidence, theory and beyond. *Earth Surface Processes and Landforms*, 39(1), 38–61. <https://doi.org/10.1002/esp.3462>
- Martinez-Gutierrez, G., & Sethi, P. (1997). Miocene-Pleistocene sediments within the San Jose del Cabo Basin, Baja California Sur, Mexico. In *Pliocene carbonates and related facies flanking the Gulf of California, Baja California, Mexico* (318th ed., pp. 141–166). Geological Society of America Special Paper.
- Miller, S. R., & Slingerland, R. L. (2006). Topographic advection on fault-bend folds: Inheritance of valley positions and the formation of wind gaps. *Geology*, 34(9), 769. <https://doi.org/10.1130/G22658.1>
- Miller, S. R., Slingerland, R. L., & Kirby, E. (2007). Characteristics of steady state fluvial topography above fault-bend folds. *Journal of Geophysical Research*, 112(F4), F04004. <https://doi.org/10.1029/2007JF000772>
- Mitchell, N., & Forte, A. M. (2023). Tectonic advection of contacts enhances landscape transience. *Earth Surface Processes and Landforms*, 48(7), 1450–1469. <https://doi.org/10.1002/esp.5559>
- Montgomery, D. R., & Foufoula-Georgiou, E. (1993). Channel network source representation using digital elevation models. *Water Resources Research*, 29(12), 3925–3934. <https://doi.org/10.1029/93WR02463>
- Mudd, S. M., Clubb, F., Grieve, S., Milodowski, D., Gailleron, B., Hurst, M., et al. (2022). LSDtopools/LSDTopoTools2: LSDTopoTools2 v0.7. *Zenodo*. <https://doi.org/10.5281/zenodo.7076014>
- Mudd, S. M., Attal, M., Milodowski, D. T., Grieve, S. W. D., & Valters, D. A. (2014). A statistical framework to quantify spatial variation in channel gradients using the integral method of channel profile analysis. *Journal of Geophysical Research: Earth Surface*, 119(2), 138–152. <https://doi.org/10.1002/2013JF002981>
- Mudd, S. M., Clubb, F. J., Gailleron, B., & Hurst, M. D. (2018). How concave are river channels? *Earth Surface Dynamics*, 6(2), 505–523. <https://doi.org/10.5194/esurf-6-505-2018>
- Mudd, S. M., Roda-Boluda, D. C., Goren, L., & Clubb, F. J. (2022). Beyond the long profile. In *Treatise on geomorphology* (pp. 22–52). Elsevier. <https://doi.org/10.1016/B978-0-12-818234-5.00026-2>
- Ortega-Gutiérrez, F., Elías-Herrera, M., Morán-Zenteno, D. J., Solari, L., Luna-González, L., & Schaaf, P. (2014). A review of batholiths and other plutonic intrusions of Mexico. *Gondwana Research*, 26(3–4), 834–868. <https://doi.org/10.1016/j.gr.2014.05.002>
- Perron, J. T., Kirchner, J. W., & Dietrich, W. E. (2009). Formation of evenly spaced ridges and valleys. *Nature*, 460(7254), 502–505. <https://doi.org/10.1038/nature08174>
- Perron, J. T., & Royden, L. (2013). An integral approach to bedrock river profile analysis. *Earth Surface Processes and Landforms*, 38(6), 570–576. <https://doi.org/10.1002/esp.3302>

- Roering, J. J., Kirchner, J. W., & Dietrich, W. E. (1999). Evidence for nonlinear, diffusive sediment transport on hillslopes and implications for landscape morphology. *Water Resources Research*, 35(3), 853–870. <https://doi.org/10.1029/1998wr900090>
- Roering, J. J., Kirchner, J. W., & Dietrich, W. E. (2001). Hillslope evolution by nonlinear, slope-dependent transport: Steady state morphology and equilibrium adjustment timescales. *Journal of Geophysical Research*, 106(B8), 16499–16513. <https://doi.org/10.1029/2001jb000323>
- Rowan, A. V., Plummer, M. A., Brocklehurst, S. H., Jones, M. A., & Schultz, D. M. (2013). Drainage capture and discharge variations driven by glaciation in the Southern Alps, New Zealand. *Geology*, 41(2), 199–202. <https://doi.org/10.1130/G33829.1>
- Royden, L., Clark, M., & Whipple, K. (2000). Evolution of river elevation profiles by bedrock incision: Analytical solutions for transient river profiles related to changing uplift and precipitation rates. In *EOS, trans, American geophysical union*. (Vol. 81)
- Schwanghart, W., & Scherler, D. (2020). Divide mobility controls knickpoint migration on the Roan Plateau (Colorado, USA). *Geology*, 48(7), 698–702. <https://doi.org/10.1130/G47054.1>
- Seidl, M., & Dietrich, W. E. (1992). The problem of channel erosion into bedrock. *Catena Supplement*, 23, 101–124.
- Shelef, E., & Goren, L. (2021). The rate and extent of wind-gap migration regulated by tributary confluences and avulsions. *Earth Surface Dynamics*, 9(4), 687–700. <https://doi.org/10.5194/esurf-9-687-2021>
- Shi, F., Tan, X., Zhou, C., & Liu, Y. (2021). Impact of asymmetric uplift on mountain asymmetry: Analytical solution, numerical modeling, and natural examples. *Geomorphology*, 389, 107862. <https://doi.org/10.1016/j.geomorph.2021.107862>
- Shugar, D. H., Clague, J. J., Best, J. L., Schoof, C., Willis, M. J., Copland, L., & Roe, G. H. (2017). River piracy and drainage basin reorganization led by climate-driven glacier retreat. *Nature Geoscience*, 10(5), 370–375. <https://doi.org/10.1038/ngeo2932>
- Stokes, M. F., Goldberg, S. L., & Perron, J. T. (2018). Ongoing River capture in the Amazon. *Geophysical Research Letters*, 45(11), 5545–5552. <https://doi.org/10.1029/2018GL078129>
- Talling, P. J., Stewart, M. D., Stark, C. P., Gupta, S., & Vincent, S. J. (1997). Regular spacing of drainage outlets from linear fault blocks. *Basin Research*, 9(4), 275–302. <https://doi.org/10.1046/j.1365-2117.1997.00048.x>
- Tucker, G. E., Lancaster, S. T., Gasparini, N. M., Bras, R. L., & Rybarczyk, S. M. (2001). An object-oriented framework for distributed hydrologic and geomorphic modeling using triangulated irregular networks. *Computers & Geosciences*, 27(8), 959–973. [https://doi.org/10.1016/S0098-3004\(00\)00134-5](https://doi.org/10.1016/S0098-3004(00)00134-5)
- Tucker, G. E., & Whipple, K. X. (2002). Topographic outcomes predicted by stream erosion models: Sensitivity analysis and intermodel comparison. *Journal of Geophysical Research*, 107(B9), ETG1-1–ETG1-16. <https://doi.org/10.1029/2001JB000162>
- Whipple, K. X. (2004). Bedrock rivers and the geomorphology of active orogens. *Annual Review of Earth and Planetary Sciences*, 32(1), 151–185. <https://doi.org/10.1146/annurev.earth.32.101802.120356>
- Whipple, K. X., DiBiase, R. A., Ouimet, W. B., & Forte, A. M. (2017). Preservation or piracy: Diagnosing low-relief, high-elevation surface formation mechanisms. *Geology*, 45(1), 91–94. <https://doi.org/10.1130/G38490.1>
- Whipple, K. X., Forte, A. M., DiBiase, R. A., Gasparini, N. M., & Ouimet, W. B. (2017). Timescales of landscape response to divide migration and drainage capture: Implications for the role of divide mobility in landscape evolution. *Journal of Geophysical Research: Earth Surface*, 122(1), 248–273. <https://doi.org/10.1002/2016JF003973>
- Whipple, K. X., & Tucker, G. E. (1999). Dynamics of the stream-power river incision model: Implications for height limits of mountain ranges, landscape response timescales, and research needs. *Journal of Geophysical Research*, 104(B8), 17661–17674. <https://doi.org/10.1029/1999JB900120>
- Willett, S. D. (1999). Orogeny and orography: The effects of erosion on the structure of mountain belts. *Journal of Geophysical Research*, 104(B12), 28957–28981. <https://doi.org/10.1029/1999JB900248>
- Willett, S. D., & Brandon, M. T. (2002). On steady states in mountain belts. *Geology*, 30(2), 175. [https://doi.org/10.1130/0091-7613\(2002\)030\(0175:OSSIMB\)2.0.CO;2](https://doi.org/10.1130/0091-7613(2002)030(0175:OSSIMB)2.0.CO;2)
- Willett, S. D., McCoy, S. W., Perron, J. T., Goren, L., & Chen, C.-Y. (2014). Dynamic reorganization of river basins. *Science*, 343(6175), 1248765. <https://doi.org/10.1126/science.1248765>
- Willett, S. D., Slingerland, R., & Hovius, N. (2001). Uplift, shortening, and steady state topography in active mountain belts. *American Journal of Science*, 301(4–5), 455–485. <https://doi.org/10.2475/ajs.301.4-5.455>
- Wobus, C., Whipple, K. X., Kirby, E., Snyder, N., Johnson, J., Spyropoulos, K., et al. (2006). Tectonics from topography: Procedures, promise, and pitfalls. In *Tectonics, climate, and landscape evolution*. Geological Society of America. [https://doi.org/10.1130/2006.2398\(04\)](https://doi.org/10.1130/2006.2398(04))
- Yang, R., Willett, S. D., & Goren, L. (2015). In situ low-relief landscape formation as a result of river network disruption. *Nature*, 520(7548), 526–529. <https://doi.org/10.1038/nature14354>
- Zhou, C., Tan, X., Liu, Y., & Shi, F. (2022). A cross-divide contrast index (C) for assessing controls on the main drainage divide stability of a mountain belt. *Geomorphology*, 398, 108071. <https://doi.org/10.1016/j.geomorph.2021.108071>